Front. Mech. Eng. 2023, 18(3): 37
https://doi.org/10.1007/s11465-023-0753-3

RESEARCH ARTICLE

Obstacle-circumventing adaptive control of a four-wheeled mobile robot subjected to motion uncertainties

Yiming YAN[a], Shuting WANG[a], Yuanlong XIE (✉)[a], Hao WU[a], Shiqi ZHENG[b,c], Hu LI[a]

[a] *School of Mechanical Science and Engineering, Huazhong University of Science and Technology, Wuhan 430074, China*
[b] *School of Automation, China University of Geosciences, Wuhan 430074, China*
[c] *Hubei Key Laboratory of Advanced Control and Intelligent Automation for Complex Systems, Wuhan 430074, China*
✉ *Corresponding author. E-mail: yuanlongxie@hust.edu.cn (Yuanlong XIE)*

ABSTRACT To achieve the collision-free trajectory tracking of the four-wheeled mobile robot (FMR), existing methods resolve the tracking control and obstacle avoidance separately. Guaranteeing the synergistic robustness and smooth navigation of mobile robots subjected to motion uncertainties in a dynamic environment using this non-cooperative processing method is difficult. To address this challenge, this paper proposes an obstacle-circumventing adaptive control (OCAC) framework. Specifically, a novel anti-disturbance terminal slide mode control with adaptive gains is formulated, incorporating specified control laws for different stages. This formulation guarantees rapid convergence and simultaneous chattering elimination. By introducing sub-target points, a new sub-target dynamic tracking regression obstacle avoidance strategy is presented to transfer the obstacle avoidance problem into a dynamic tracking one, thereby reducing the burden of local path searching while ensuring system stability during obstacle circumvention. Comparative experiments demonstrate that the proposed OCAC method can strengthen the convergence and obstacle avoidance efficiency of the concerned FMR system.

KEYWORDS four-wheeled mobile robot, obstacle-circumventing adaptive control, adaptive anti-disturbance terminal sliding mode control, sub-target dynamic tracking regression obstacle avoidance

1 Introduction

Owing to their operational flexibility and short deployment time, mobile robots are widely used in labor-intensive manufacturing applications [1,2]. To date, different mobile robots have been developed to facilitate trajectory tracking through the coordinated regulation of wheel modules, such as differential, steering, and Mecanum wheeled robots [3]. However, these mobile robots have a common drawback, that is, they are always limited by operating angle constraints when performing complex trajectory tracking while circumventing obstacles [4]. In contrast, a four-wheeled mobile robot (FMR) can overcome these angle constraints and achieve smooth angle steering in complex scenes [5,6] because of the independent drive characteristics of in-wheel and steering motors. The FMR exhibits excellent adaptability to industrial scenarios characterized by harsh ground conditions and confined spaces that necessitate high flexibility. Nonetheless, in complex dynamic operating scenarios, environmental or state uncertainties may significantly affect its high-precision trajectory tracking and obstacle circumvention [5], which cannot be ignored.

To realize real-time trajectory tracking with synchronous obstacle circumventing, most modern approaches used in tracking resolution separate the collision-free planning from the process of tracking the predefined path. In this way, dynamic obstacle interference can easily cause FMR to deviate from the originally planned optimal path, thereby reducing the adaptability of FMR to dynamic environments. For example, in Ref. [7], the research on the obstacle avoidance strategies of mobile robots lacked the coordination of tracking methods. In Ref. [8], a fault-tolerant controller (FTC) was proposed to ensure system security and state convergence step by step by initially generating a feasible control strategy. In Ref. [9], a tracking control framework was formulated using a trajectory generation method and a common sliding mode control, which was selected to translate the trajectory tracking errors into the reference values of the tire force

Received November 15, 2022; accepted March 13, 2023

distributor. To enhance the accuracy of tracking unmanned vehicles on known trajectories, two optimized model predictive control (MPC) trajectory tracking control systems are designed in Ref. [10] based on the adaptive compensation and robust control of a radial basis function (RBF) neural network. However, these methods cannot accommodate real-time demand for tracking with asynchronous offline planning when encountering a new obstacle, which is computationally extensive and time consuming. Notably, deep learning methods that use neural network models are commonly used to deal with trajectory tracking problems considering obstacle avoidance. For instance, in Ref. [11], a metaheuristic-based control framework is proposed to improve obstacle avoidance capabilities during the of tracking predefined reference paths by introducing a combined penalty term into the objective function. Furthermore, in terms of the characteristics of FMR working conditions, such as small-scale buffer space [6] and fast response requirement [5], the development of an accurate tracking control framework that incorporates timely obstacle circumvention becomes crucial for performance optimization. However, the research on superior obstacle-circumventing tracking control is still confronted with considerable challenges that range from control law performance to collision-free capability.

Currently, considerable efforts, such as proportional–integral–derivative (PID) control, MPC, scroll optimization control, and sliding mode control (SMC), are devoted to the tracking control of mobile robots. Among these methods, SMC exhibits unique advantages in ensuring fast convergence features and robustness of mobile robots with time-varying model turbulence due to its insensitivity to system uncertainties and unknown disturbances [12]. SMC offers alternative options in designing appropriate adaptive parameters, thus satisfying an ever-increasing appeal for the high-precision and high-efficiency control of mobile robots under environmental and state uncertainties [13]. In Ref. [14], a reduced-order extended state observer (ESO) based SMC scheme is applied to compensate for friction in a three-wheeled omnidirectional mobile robot. A sliding mode controller with adaptive gains for trajectory tracking of unicycle mobile robots is propounded by Ref. [15]. Similarly, in Ref. [16], a new control strategy that combines high-order disturbance observer and sliding model control for the balance and speed control of the mobile wheeled inverted pendulum system is proposed. Given its ease of improvement and implementation, SMC can be significantly applied to the concerned FMR [5,6]. However, existing sliding mode tracking control schemes still have limitations in dealing with the disturbances of mobile robots [17,18], which run counter to the actual situation and pose a challenge in developing an enhanced control framework based on the proposed FMR.

The main challenge in existing SMC is finding a balance between convergence speed and stability, as rapid convergence can easily lead to system oscillation. In Ref. [19], the use of the single SMC law in the entire SMC stage failed to achieve balance between speed and chattering mitigation due to the nonlinear and discontinuous characteristics of FMR. When SMC is far from the sliding mode surface, the system is expected to converge with a fast convergence rate to ensure the rapid system response [20]. When approaching the sliding mode surface, the system must reduce the convergence and oscillation to smoothly tend to the sliding mode surface and ensure the system robustness [21]. To address this problem, many scholars have presented some solutions. For example, in Ref. [22], a variable-structure SMC is utilized to manage the azimuth angle and lateral position deviation of the autonomous vehicle, thereby enhancing the system’s robustness on the sliding mode surface. In Ref. [23], an impulsive adaptive super-twisting SMC algorithm is introduced to drive the state vector to the origin in a short time and keep it there despite the presence of disturbances. As proposed in Ref. [24], the effects of reaching phase issue and chattering in conventional optimal integral SMC are significantly addressed by representing the system dynamics in the error coordinate and introducing an additional optimal integral term [25]. The robust finite-time rendezvous maneuver control for spacecraft is investigated by designing a new type of sliding mode surface and modifying the control law while considering to reduce the influence of chatter. In Ref. [26], chattering is completely eliminated without overestimating the control gains by adopting an adaptive continuous barrier function in the dynamic switching function. Nonlinear systems in Ref. [27] are not only capable of estimating unknown disturbance but are also capable of alleviating the chattering problem in the control signal by designing a new form of combined observer-controller. However, the abovementioned methods depend on the specific constraints of the motion model, which is unsuitable to the formulated FMR. Thus, appropriate control law research design is of great significance to the proposed FMR, which also prompts us to study here.

As an essential subprocess of the tracking control framework, significant attention has been given to the obstacle circumventing problem. The research on the trajectory obstacle planning method is extensive. For instance, an artificial potential field (APF) obstacle avoidance method based on decision-making force is proposed to ensure the safety and flexibility of a robotic arm in complex scenarios [28]. In Ref. [29], a novel motion planning framework is proposed for automated vehicles based on APF elaborated resistance approach to help vehicles drive safely, comfortably, economically, and human-like. The vector field histogram (VFH/VFH+) algorithm can consider the specific kinematic characteristics of mobile robots and pay attention to handling uncertainties from sensors and modeling errors, so that it can be well applied to the obstacle circumvention regression of mobile robots [30]. In Ref. [31], the author proposes a finite distribution estimation-based dynamic window approach to avoid dynamic obstacles by estimating the overall distribution of obstacles. Research detailed in Ref. [32] illustrates how a remote center of movement (RCM) strategy could be used to avoid collisions while working with small openings. However, existing obstacle avoidance algorithms only consider avoiding obstacles, without comprehensively considering the combination of the replanned path after obstacle avoidance and the original path [33]. Typically, due to the increase in the constraint level, the local planner must obtain feedback at a higher rate during fine motion, which increases the computational cost of the system [34]. The need to replan the remaining paths after obstacle avoidance greatly reduces the utilization efficiency of system planning resources. In addition, existing obstacle circumvention strategies are usually adapted to differential robots [35], single/dual steering wheel robots [36], and intelligent road vehicles [37]. Limited research on four-wheel driving robots, such as FMR, exists. The FMR boasts a distinctive design, incorporating a top-loading feature and a substantial size that limits its maneuverability and prevents it from making abrupt changes in direction. Its significant mass makes it unsuitable for utilizing standard obstacle avoidance techniques [38]. Therefore, the FMR-suitable obstacle circumvention algorithm for dynamic obstacles is critical for the performance of trajectory tracking control framework.

Motivated by the above analysis, this paper proposes an obstacle-circumventing adaptive control (OCAC) framework under motion uncertainties. Compared with existing control strategies, the key contributions of this control scheme are mainly outlined as follows:

(1) In contrast to the abovementioned control schemes, such as Ref. [9], the OCAC framework integrates the obstacle circumvention into the real-time trajectory tracking process. This integration overcomes drawbacks, such as high calculation and slow responses associated with asynchronous operation. Meanwhile, based on the kinematics–dynamics hierarchical control approach, this paper realizes the precise control of trajectory tracking accuracy by analyzing the FMR kinematics module while ensuring the basic angle-motor torque control.

(2) By combining a proportional–integral sliding mode surface and a gain-adaptive control law, an anti-disturbance terminal slide mode control with adaptive gains (ADTSMCAGs) is proposed. In contrast to existing single-form control laws [5], the proposed SMC with adaptive gains guarantees the rapid system convergence and chattering mitigation when the system approaches the sliding mode surface.

(3) A novel sub-target dynamic tracking regression obstacle avoidance (SDTROA) strategy is proposed for the real-time trajectory re-planning of FMR. By utilizing the specific sub-target dynamic tracking strategy, the FMR can efficiently return to the original path after obstacle avoidance is completed. Thus, compared with other obstacle-avoiding works, such as Ref. [33], enhances the utilization of original reference and significantly reduces the computational load of the real-time planning.

(4) In contrast to Refs. [39,41], the modified proportional−integral sliding surface and the stage-variable control law with adaptive gains can be readily implemented on the FMR platform. Following this line of thought, dynamic tracking and obstacle avoidance strategies based on actual working scenario maps are possible to achieve. The experimental results validate the superiority of the proposed control framework over conventional tracking control methods in terms of efficiency and robustness.

The remainder of this paper is organized as follows: Section 2 presents the problem to be resolved; Section 3 introduces the formulated OCAC control framework, which comprises the ADTSMCAG method and the SDTROA strategy; Sections 4 and 5 provide the experimental results and conclusions, respectively.

2 Problem statement

As illustrated in Fig. 1, the developed FMR can be configured in the variable-Ackerman steer mode. The robot state, position, and orientation are denoted as $\boldsymbol{q}$, (x, y), and θ, respectively. Then, the related kinematic states are determined by

$$\begin{aligned}\dot{\boldsymbol{q}} &= \begin{bmatrix} x & \dot{y} & \dot{\theta} \end{bmatrix} \\ &= \begin{bmatrix} V_1 \cos\theta & V_1 \sin\theta & V_1 (\tan\delta_{\mathrm{f}} - \tan\delta_{\mathrm{r}})/(L_{\mathrm{f}} + L_{\mathrm{r}}) \end{bmatrix},\end{aligned} \quad (1)$$

where V_1 denotes the linear velocity of FMR, L_{f} and L_{r} denote the distances from front and rear wheels to the robot center, respectively, and δ_{f} and δ_{r} are virtual front and rear wheel angles located on the centerline of the FMR's body, respectively.

Remark 1. The control objective of this paper is to achieve high precision in FMR trajectory tracking, which is closely related to the control of the dynamics layer and kinematics layer. Generally, the control of the dynamic layer adopts conventional PID methods, which provide strong stability and is very suitable for the high stability requirements of the torque motor. Therefore, the control method of the kinematics module is of great significance to the trajectory tracking accuracy of FMR.

Remark 2. When FMR is deployed in an engineering project to perform specific tasks, its motion must be guided along a predefined path, which requires coordination among three motion modes. In general, the variable-

Ackerman steer mode, characterized by variables δ_f and δ_r, is the preferred mode. However, when the FMR encounters sharp turns, the diagonal-move steer mode, in which the virtual front and rear wheel angles satisfy $\delta_\mathrm{f} = \delta_\mathrm{r}$, is the most appropriate. Furthermore, for typical minor turns, the variable-Ackerman steer mode transforms into the common-Ackerman steer mode, where $\delta_\mathrm{r} = 0$.

By introducing $\boldsymbol{q}_\mathrm{r}$ as the trajectory reference, we yield

$$\dot{\boldsymbol{q}}_\mathrm{r} = \begin{bmatrix} \dot{x}_\mathrm{r} & \dot{y}_\mathrm{r} & \dot{\theta}_\mathrm{r} \end{bmatrix} = \begin{bmatrix} V_\mathrm{lr}\cos\theta_\mathrm{r} & V_\mathrm{lr}\sin\theta_\mathrm{r} & \dot{\theta}_\mathrm{r} \end{bmatrix}. \quad (2)$$

As displayed in Fig. 2, $(x_\mathrm{r}, y_\mathrm{r})$ is the coordinate of the closest position on the reference trajectory selected by FMR at each moment during trajectory tracking. The reference yaw angle is not the yaw angle of the reference position. Position T is obtained by extending the unit length along the tangential direction of the reference position. The reference yaw angle θ_r is selected as the connection vector angle between position T and the actual position, which ensures that FMR can always point to the reference trajectory simultaneously. Then, we formulate θ_r as

$$\theta_\mathrm{r} = \arctan\frac{y_T - y}{x_T - x}, \quad (3)$$

$$\begin{bmatrix} x_T \\ y_T \end{bmatrix} = \begin{bmatrix} x_\mathrm{r} + \cos\theta_P \\ y_\mathrm{r} + \sin\theta_P \end{bmatrix}, \quad (4)$$

where (x_T, y_T) is the coordinate of position T and θ_P denotes the tangent direction angle of the reference position.

Furthermore, we formulate a system state–space model as follows:

$$\dot{X}_1 = \theta_\mathrm{e} = X_2, \quad (5)$$

$$\dot{X}_2 = \dot{\theta}_\mathrm{e} = \dot{\theta} - \dot{\theta}_\mathrm{r} + \gamma = \frac{V_1(\tan\delta_\mathrm{f} - \tan\delta_\mathrm{r})}{L_\mathrm{f} + L_\mathrm{r}} - \dot{\theta}_\mathrm{r} + \gamma, \quad (6)$$

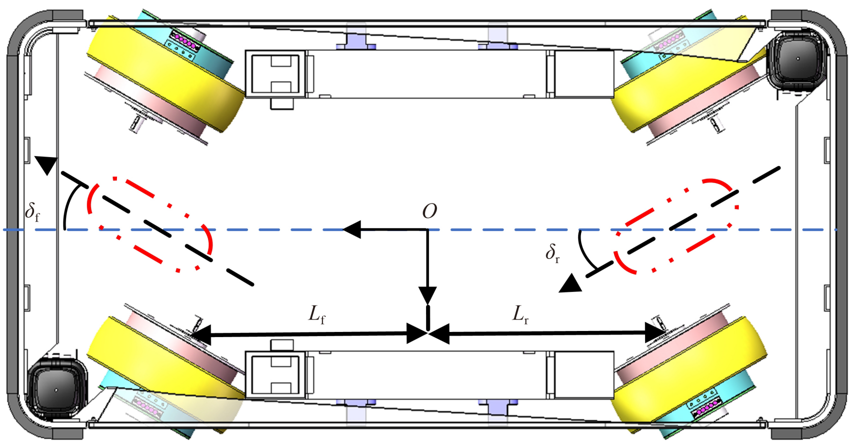

Fig. 1 Variable-Ackerman steer mode of the four-wheeled mobile robot.

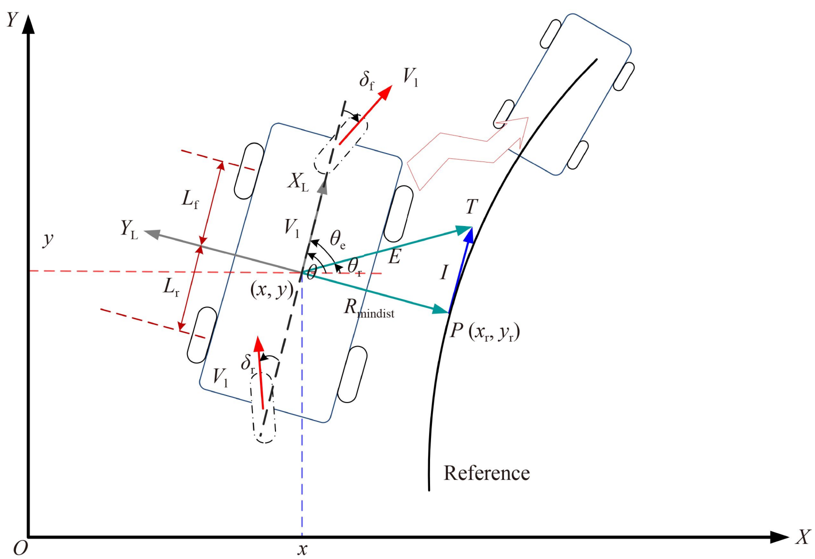

Fig. 2 Yaw angle error model of the four-wheeled mobile robot.

where X_1 and X_2 represent variables of the equations of state, $\theta_e = \theta - \theta_r$, $\gamma = \Delta_t\left(\dot{\theta} - \dot{\theta}_r\right) + \gamma'$ denotes the bounded lumped uncertainties comprising system parameter perturbations and external disturbances, Δ_t represents the system parameter perturbations, and γ' is the external disturbance.

Remark 3. In the context of trajectory tracking control for an FMR, this paper proposes a novel approach to simplify the control process by utilizing a unique reference yaw angle, denoted as θ_r, which aligns with the reference trajectory. This approach eliminates the need for the simultaneous control of position and attitude, as the control of yaw angle alone suffices to achieve the desired trajectory tracking. This results in a substantial reduction in computational cost.

Given that FMR must avoid static and dynamic obstacles in uncertain environments, we describe obstacle avoidance constraints in the form of

$$G_{i,j}^{\mathrm{ob}}(\boldsymbol{q}) = d_{i,j}^{\mathrm{ob}}(\boldsymbol{q}) - (d_s + d_{\mathrm{ero}}) \geqslant 0, \tag{7}$$

where $d_{i,j}^{\mathrm{ob}}(\boldsymbol{q}) = \sqrt{\left(x - x_{i,j}^{\mathrm{ob}}\right)^2 + \left(y - y_{i,j}^{\mathrm{ob}}\right)^2}$ is the distance from the current position of FMR to the center of the obstacle unit, d_s is the radius of the radar scanning area, and d_{ero} is the corrosion radius of the obstacle unit after considering the safety distance.

The replanned path provides FMR with a new reference path $\boldsymbol{q}_{\mathrm{rob}}$, thereby ensuring that $G_{i,j}^{\mathrm{ob}}(\boldsymbol{q}_{\mathrm{rob}}) \geqslant 0$ is for trajectory tracking. $\boldsymbol{q}_{\mathrm{rob}}$ is different from the original reference path $\boldsymbol{q}_r$, which leads to $G_{i,j}^{\mathrm{ob}}(\boldsymbol{q}_r) < 0$ without considering the obstacles that may be encountered. However, a brand-new circumventing path does not consider the computational efficiency and reaction time, which is crucial to FMR's trajectory tracking. To address this problem, the control objective here is to build a set of control strategy frameworks, which consider collision-free returning, to ensure that FMR can resume trajectory tracking rapidly and smoothly.

3 Main results

Figure 3 exhibits the OCAC control framework coupling trajectory tracking and obstacle circumvention. θ_r is used as the initial input of the framework to provide the predefined reference trajectory, which represents the optimal path in ideal conditions without obstacles and turbulence. θ_{obr} is the updated reference trajectory output by the control framework after encountering obstacle disturbance. θ is the actual tracking angle of FMR, which is subtracted from θ_r and θ_{obr} to obtain tracking error θ_e, which is the core control quantity of the control framework. The two parts of the framework, namely, the tracking control method and the obstacle circumventing strategy, are described separately in the following subsections.

3.1 Design of the ADTSMCAG

Different from the traditional linear or integral sliding surface, a modified proportion-integral sliding mode surface is designed as follows:

$$\begin{cases} S(t_n) = \chi_1\theta_e(t_n) + \int_0^{t_n} \overline{S}(k)\mathrm{d}k, \\ \overline{S}(t_n) = \chi_2\theta_e(t_n) + \chi_3|\theta_e(t_n)|^{\beta_1}\mathrm{sign}(\theta_e(t_n)) \\ \qquad + \chi_4|\theta_e(t_n)|^{\beta_2}\mathrm{sign}(\theta_e(t_n)), \end{cases} \tag{8}$$

where $S(t_n)$ and $\overline{S}(t_n)$ represent the sliding mode surface, k and t_n denote integral sliding mold surface time, $\chi_1, \chi_2, \chi_3, \chi_4 \in \mathbb{R}^+$ denote the preset control gains, and $\beta_1 \in (1, \infty)$ and $\beta_2 \in (0, 1)$ denote the predefined error coefficients. The proposed sliding mode surface in this study is formulated with a combination of proportional and integral terms to ensure rapid convergence and low steady-state error in the presence of modeling inaccuracies and continuous disturbances.

Theorem 1. Assume that the rotation angle control law of the front and rear virtual wheels of the mobile robot is

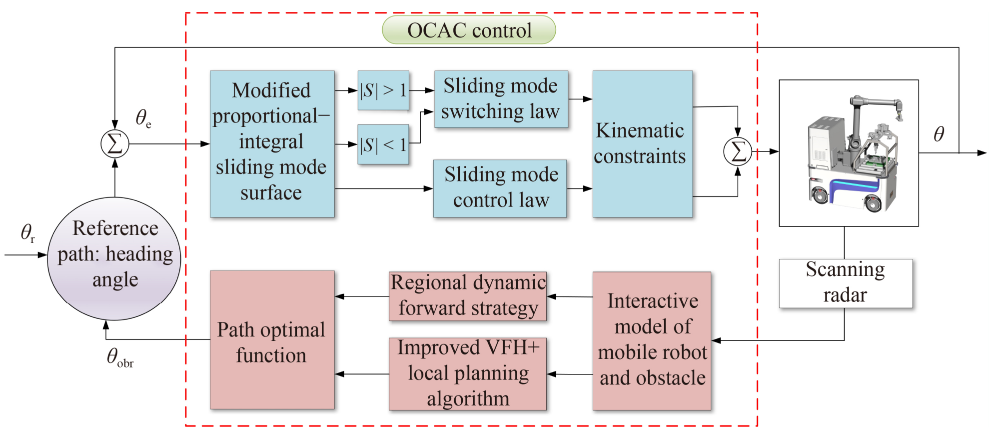

Fig. 3 Obstacle-circumventing adaptive control (OCAC) control framework.

$$\delta_{\mathrm{f}} = -\delta_{\mathrm{r}} = \tan^{-1}\frac{(L_{\mathrm{f}}+L_{\mathrm{r}})(\Xi+\Omega)}{2V_1\chi_1}, \tag{9}$$

$$\Xi = \chi_1\dot{\theta}_{\mathrm{r}} - \chi_2\theta_{\mathrm{e}} - \chi_3|\theta_{\mathrm{e}}|^{\beta_1}\operatorname{sign}(\theta_{\mathrm{e}}) - \chi_4|\theta_{\mathrm{e}}|^{\beta_2}\operatorname{sign}(\theta_{\mathrm{e}}), \tag{10}$$

$$\Omega = -h_1|S|^{q_1}\operatorname{sign}(S) - h_2|S|^{q_2}\operatorname{sign}(S) - h_3 S, \tag{11}$$

where Ξ and Ω represent the equivalent control law and reaching law, respectively, and q_1 and q_2 are positive parameters that satisfy

$$q_1 = \begin{cases} m_0 + m_1 - m_2, & \text{if } |S| \geqslant 1, \\ m_0 + \dfrac{3}{2}m_1 S^g - \dfrac{1}{2}m_1 S^{3g} - m_2\tanh(\lambda S^2), & \text{if } |S| < 1, \end{cases} \tag{12}$$

$$q_2 = \begin{cases} m_0 + m_1 - m_2, & \text{if } |S| \geqslant 1, \\ 1, & \text{if } |S| < 1, \end{cases} \tag{13}$$

$$\begin{cases} g > 2 \text{ and even, } \lambda > 0, \\ 0 < m_2 < m_0 < 1,\ m_1 > 1, \\ m_0 + m_1 - m_2 > 1, \end{cases} \tag{14}$$

where h_1, h_2, and h_3 satisfy $h_1 > \gamma\chi_1 \cdot \operatorname{sign}(S)/|S|^q$, $h_2 > 0$, and $h_3 > 0$, respectively. If the control law satisfies the aforementioned conditions, then the angular error of the mobile robot will asymptotically converge towards zero, thereby effectively achieving precise orientation control.

Proof: Derivative Eq. (8) in time domain yields

$$\dot{S} = \chi_1\dot{\theta}_{\mathrm{e}} + \chi_2\theta_{\mathrm{e}} + \chi_3|\theta_{\mathrm{e}}|^{\beta_1}\operatorname{sign}(\theta_{\mathrm{e}}) + \chi_4|\theta_{\mathrm{e}}|^{\beta_2}\operatorname{sign}(\theta_{\mathrm{e}}). \tag{15}$$

Substituting Eq. (6) into Eq. (15) results in

$$\begin{aligned}\dot{S} &= \chi_1\left(\frac{V_1(\tan\delta_{\mathrm{f}} - \tan\delta_{\mathrm{r}})}{L_{\mathrm{f}}+L_{\mathrm{r}}} - \dot{\theta}_{\mathrm{r}} + \gamma\right) + \chi_2\theta_{\mathrm{e}} \\ &\quad + \chi_3|\theta_{\mathrm{e}}|^{\beta_1}\operatorname{sign}(\theta_{\mathrm{e}}) + \chi_4|\theta_{\mathrm{e}}|^{\beta_2}\operatorname{sign}(\theta_{\mathrm{e}}).\end{aligned} \tag{16}$$

From Eq. (9), we can obtain

$$\begin{aligned}\tan\delta_{\mathrm{f}} - \tan\delta_{\mathrm{r}} &= \frac{(L_{\mathrm{f}}+L_{\mathrm{r}})(\Xi+\Omega)}{2V_1\chi_1} - \left(-\frac{(L_{\mathrm{f}}+L_{\mathrm{r}})(\Xi+\Omega)}{2V_1\chi_1}\right) \\ &= \frac{(L_{\mathrm{f}}+L_{\mathrm{r}})(\Xi+\Omega)}{V_1\chi_1}.\end{aligned} \tag{17}$$

The combination of Eqs. (16) and (17) leads to

$$\begin{aligned}\dot{S} &= \chi_1\left(\frac{V_1}{L_{\mathrm{f}}+L_{\mathrm{r}}}\frac{(L_{\mathrm{f}}+L_{\mathrm{r}})(\Xi+\Omega)}{2V_1\chi_1} - \dot{\theta}_{\mathrm{r}}\right) + \gamma\chi_1 + \chi_2\theta_{\mathrm{e}} \\ &\quad + \chi_3|\theta_{\mathrm{e}}|^{\beta_1}\operatorname{sign}(\theta_{\mathrm{e}}) + \chi_4|\theta_{\mathrm{e}}|^{\beta_2}\operatorname{sign}(\theta_{\mathrm{e}}) \\ &= \chi_1\left(\Xi + \Omega - \dot{\theta}_{\mathrm{r}} + \gamma\right) + \chi_2\theta_{\mathrm{e}} + \chi_3|\theta_{\mathrm{e}}|^{\beta_1}\operatorname{sign}(\theta_{\mathrm{e}}) \\ &\quad + \chi_4|\theta_{\mathrm{e}}|^{\beta_2}\operatorname{sign}(\theta_{\mathrm{e}}) \\ &= \gamma\chi_1 - h_1|S|^{q_1}\operatorname{sign}(S) - h_2|S|^{q_2}\operatorname{sign}(S) - h_3 S.\end{aligned} \tag{18}$$

Let us consider a Lyapunov candidate

$$V = \frac{1}{2}S^2. \tag{19}$$

Combining Eqs. (18) and (19), we obtain

$$\begin{aligned}\dot{V} = S\cdot\dot{S} &= S\cdot(\gamma\chi_1 - h_1|S|^{q_1}\operatorname{sign}(S) - h_2|S|^{q_2}\operatorname{sign}(S) - h_3 S) \\ &= -h_1 S\cdot|S|^{q_1}\operatorname{sign}(S) - h_2 S\cdot|S|^{q_2}\operatorname{sign}(S) - h_3 S^2 + \gamma\chi_1\cdot S \\ &\leqslant -h_1 S\cdot|S|^{q_1}\operatorname{sign}(S) - h_2 S\cdot|S|^{q_2}\operatorname{sign}(S) + \gamma\chi_1\cdot S \\ &= -h_1|S|^{q_1+1} - h_2|S|^{q_2+1} + \gamma\chi_1\cdot S.\end{aligned} \tag{20}$$

Consider the relationship between the parameters and the upper bound of the error

$$h_1 > \frac{\gamma\chi_1\cdot\operatorname{sign}(S)}{|S|^q} \to h_1|S|^{q_1+1} > \gamma\chi_1\cdot S. \tag{21}$$

Therefore, we can obtain the following:

$$\begin{aligned}\dot{V} &\leqslant -h_1|S|^{q_1+1} - h_2|S|^{q_2+1} + \gamma\chi_1\cdot S \\ &= -h_2|S|^{q_2+1} - \left(h_1|S|^{q_1+1} - \gamma\chi_1\cdot S\right).\end{aligned} \tag{22}$$

From Eq. (22), we conclude that $\dot{V} \leqslant 0$. Also, the Lyapunov condition of the entire closed-loop SMC system is satisfied, that is, the sliding mode surface will ultimately converge towards zero, resulting in a stable and effective control performance. Here, the proof is completed.

Remark 4. The proposed SMC law is regulated for the reaching and switching phases. Before reaching the sliding mode surface, the control law is designed as $\delta_{\mathrm{f}} = \tan^{-1}[(L_{\mathrm{f}}+L_{\mathrm{r}})\Omega/(2V_1\chi_1)]$, which enables the system to approach the sliding mode surface rapidly. After reaching the sliding mode surface, we revise the control law as $\delta_{\mathrm{f}} = \tan^{-1}[(L_{\mathrm{f}}+L_{\mathrm{r}})\Xi/(2V_1\chi_1)]$, ensuring that the system is stable on the sliding mode surface, and the error gradually converges to zero.

Remark 5. The reaching law is given by $\Omega = -h_1|S|^{q_1}\operatorname{sign}(S) - h_2|S|^{q_2}\operatorname{sign}(S) - h_3 S$; when the sliding mode surface $|S| > 1$, the reaching law is large, which enables the system to approach the sliding mode surface rapidly. When the sliding mode surface $|S| < 1$, the signed function term in the reaching law decreases to ensure smooth convergence to the sliding mode surface.

Theorem 2. If control law Eq. (9) can be satisfied, then the system can approach the sliding mode surface in a finite time.

Proof: According to the theorem, when $S \geqslant 0$, the designed sliding mode reaching law is the same as the switching manifold

$$\dot{S} = \Omega = -h_1|S|^{q_1}\operatorname{sign}(S) - h_2|S|^{q_2}\operatorname{sign}(S) - h_3 S. \tag{23}$$

After integrating Eq. (23), it offers

$$\int_0^{t_{\mathrm{reach}}} \mathrm{d}t = \int_{t_{\mathrm{reach}}}^{0} \frac{\dot{S}\mathrm{d}t}{h_1|S|^{q_1}\operatorname{sign}(S) + h_2|S|^{q_2}\operatorname{sign}(S) + h_3 S}, \tag{24}$$

where t_{reach} indicates the time to reach the sliding surface.

Considering q_1 and q_2 to divide the parameter value of the sliding surface $|S| = 1$, the integration process can be divided into two stages, namely, $|S| > 1$ and $0 < |S| < 1$.

Stage 1: When the sliding surface meets $|S| > 1$, coefficients q_1 and q_2 satisfy $q_1 = q_2 = m_0 + m_1 - m_2$, which are defined as q_0. Equation (24) can be expressed as follows:

$$\int_0^{t_1} \mathrm{d}t = \int_{t_1}^{0} \frac{\dot{S}\mathrm{d}t}{(h_1+h_2)|S|^{q_0}\operatorname{sign}(S)+h_3 S}$$
$$= \int_1^{S(0)} \frac{\mathrm{d}|S|}{(h_1+h_2)|S|^{q_0}+h_3|S|} \leqslant \int_1^{S(0)} \frac{\mathrm{d}|S|}{(h_1+h_2+h_3)|S|}, \tag{25}$$

where S is a function of time t and $S(0)$ is the state of the sliding surface at time $t=0$.

From Eq. (25), t_1 can be obtained as follows:

$$t_1 \leqslant \frac{\ln S(0)}{h_1+h_2+h_3}. \tag{26}$$

Stage 2: Once the sliding surface enters the area that $0<|S|<1$, q_1 and q_2 also change to the situation that $q_1 \approx m_0-m_2$, $q_2=1$. We reformulate Eq. (24) as follows:

$$\int_0^{t_2} \mathrm{d}t \approx \int_{t_2}^{0} \frac{\dot{S}\mathrm{d}t}{h_1|S|^{m_0-m_2}\operatorname{sign}(S)+h_2|S|\operatorname{sign}(S)+h_3 S}$$
$$= \int_0^{1} \frac{\mathrm{d}|S|}{h_1|S|^{m_0-m_2}+h_2|S|+h_3|S|}. \tag{27}$$

From Eq. (27), we obtain

$$t_2 \approx \frac{\ln(h_1+h_2+h_3)-\ln(h_2+h_3)}{h_1(1-m_0+m_2)}. \tag{28}$$

Combining the above two stages, for the sliding surface from $|S|=|S(0)|>0$ to $S=0$, the total convergence time is

$$t=t_1+t_2 \leqslant \frac{\ln S(0)}{h_1+h_2+h_3}+\frac{\ln(h_1+h_2+h_3)-\ln(h_2+h_3)}{h_1(1-m_0+m_2)}. \tag{29}$$

Therefore, the proposed control law ensures that the sliding mode surface converges to zero in a finite time. Here, the proof is completed.

Theorem 3. When the sliding mode surface reaches $S=0$ under the control of the proposed ADTSMCAG law, the controlled variable angle θ_e can converge to zero area in a finite time.

Proof: When the system reaches the sliding surface, the sliding surface can be described as follows:

$$\dot{S}=\chi_1\dot{\theta}_\mathrm{e}+\chi_2\theta_\mathrm{e}+\chi_3|\theta_\mathrm{e}|^{\beta_1}\operatorname{sign}(\theta_\mathrm{e})+\chi_4|\theta_\mathrm{e}|^{\beta_2}\operatorname{sign}(\theta_\mathrm{e}). \tag{30}$$

When the sliding surface satisfies $S=0$, Eq. (30) can be expressed as follows:

$$\chi_1\dot{\theta}_\mathrm{e}+\chi_2\theta_\mathrm{e}+\chi_3|\theta_\mathrm{e}|^{\beta_1}\operatorname{sign}(\theta_\mathrm{e})+\chi_4|\theta_\mathrm{e}|^{\beta_2}\operatorname{sign}(\theta_\mathrm{e})=0. \tag{31}$$

Then, error derivative $\dot{\theta}_\mathrm{e}$ can be described as follows:

$$\dot{\theta}_\mathrm{e}=\frac{-\chi_2\theta_\mathrm{e}-\chi_3|\theta_\mathrm{e}|^{\beta_1}\operatorname{sign}(\theta_\mathrm{e})-\chi_4|\theta_\mathrm{e}|^{\beta_2}\operatorname{sign}(\theta_\mathrm{e})}{\chi_1}. \tag{32}$$

Design a Lyapunov function:

$$V=\frac{1}{2}{\theta_\mathrm{e}}^2,\ \dot{V}=\theta_\mathrm{e}\cdot\dot{\theta}_\mathrm{e}. \tag{33}$$

The combination of Eqs. (32) and (33) yields

$$\dot{V}=\theta_\mathrm{e}\cdot\dot{\theta}_\mathrm{e}=\theta_\mathrm{e}\cdot\frac{-\chi_2\theta_\mathrm{e}-\chi_3|\theta_\mathrm{e}|^{\beta_1}\operatorname{sign}(\theta_\mathrm{e})-\chi_4|\theta_\mathrm{e}|^{\beta_2}\operatorname{sign}(\theta_\mathrm{e})}{\chi_1}$$
$$=-\frac{\chi_2\theta_\mathrm{e}^2}{\chi_1}-\frac{\chi_3|\theta_\mathrm{e}|^{\beta_1+1}}{\chi_1}-\frac{\chi_4|\theta_\mathrm{e}|^{\beta_2+1}}{\chi_1}\leqslant 0. \tag{34}$$

Thus, the trajectory tracking angle error θ_e can be gradually shown to converge towards zero.

From Eq. (34), we can obtain

$$\dot{V}=-\frac{\chi_2\theta_\mathrm{e}^2}{\chi_1}-\frac{\chi_3|\theta_\mathrm{e}|^{\beta_1+1}}{\chi_1}-\frac{\chi_4|\theta_\mathrm{e}|^{\beta_2+1}}{\chi_1}\leqslant-\frac{\chi_3|\theta_\mathrm{e}|^{\beta_2+1}}{\chi_1}. \tag{35}$$

Substituting $|\theta_\mathrm{e}|^2=2V$ into Eq. (35) obtains

$$\dot{V}\leqslant-\frac{2^{\frac{\beta_2+1}{2}}\chi_3 V^{\frac{\beta_2+1}{2}}}{\chi_1}. \tag{36}$$

According to Eq. (36), Eq. (32) can converge to zero in finite time, and its maximum convergence time can be obtained as follows

$$T_{\max}\leqslant{\beta_2}^{-1}(1-\beta_2)^{-1}|\theta_\mathrm{e}|^{1-\beta_2}. \tag{37}$$

Here is the complete proof.

Remark 6. A novel fuzzy control system is formulated to adjust h_1 and h_2 to balance the fast convergence and the non-tremor, respectively. The specific fuzzy rules are designed as $RULE(i)$: *IF* $S\cdot\dot{S}$ is $A^i_{s\dot{s}}$, *THEN* h_1 is $B^i_{h_1}$, h_2 is $B^i_{h_2}$, where $A^i_{s\dot{s}}$, $B^i_{h_1}$, and $B^i_{h_2}$ represent the fuzzy set of system input and system output, respectively. The center of gravity method is used to de-fuzzify the fuzzy system in the form of $h_1^{\mathrm{fz}}(S\cdot\dot{S})=\sum_{i=1}^{m}\left(\varpi_{A^i_{s\dot{s}}}\times\nu_{B^i_{h_1}}\right)\Big/\sum_{i=1}^{m}\varpi_{A^i_{s\dot{s}}}$ and $h_2^{\mathrm{fz}}(S\cdot\dot{S})=\sum_{i=1}^{m}\left(\varpi_{A^i_{s\dot{s}}}\times\nu_{B^i_{h_2}}\right)\Big/\sum_{i=1}^{m}\varpi_{A^i_{s\dot{s}}}$, where $\varpi_{A^i_{s\dot{s}}}$, $\nu_{B^i_{h_1}}$, and $\nu_{B^i_{h_2}}$ are the membership degrees of the premise and conclusion in $RULE(i)$, respectively. Specifically, the design of $\nu_{B^i_{h_1}}$ must ensure that h_1 meets the preset condition $h_1>\gamma\chi_1\cdot\operatorname{sign}(S)/|S|^q$.

Remark 7. The utilization of fuzzy logic in the design of the control system serves to mitigate the steady-state chattering and enhance the convergence speed of SMC. When the control gain satisfies the finite-time convergence condition, the integration of fuzzy logic guarantees that the steady-state oscillation of the system is limited to a small finite range near zero, leading to improved stability and performance. In addition, there are some other methods, as that shown in Ref. [42], that can solve the chattering problem by modifying sign with boundary layer methods, such as *sat* function or tanh function.

3.2 SDTROA strategy design

The subject of this study is an FMR that follows a predefined reference trajectory, until obstacles are encountered. In such cases, the reference trajectory must be altered to ensure collision-free tracking. To address this issue, the study proposes an innovative strategy known as the SDTROA approach. Once the obstacle avoidance maneuver has been executed, the goal is for the FMR to return to its original trajectory seamlessly and swiftly, continuing its pre-determined path. The design of the SDTROA approach is broken down into three key components: (1) The construction of an interactive model that encompasses the FMR and obstacles, (2) the development of a dynamic tracking strategy for sub-target points, and (3) the enhancement of the VFH+ local planning algorithm to support improved navigation.

3.2.1 Interactive model of FMR and obstacle

To enable effective obstacle avoidance, acquiring real-time environmental information is crucial. Thus, the establishment of an interactive model between the FMR and obstacles is paramount. In this study, the FMR employs a sensing strategy that utilizes a combination of LiDAR and infrared sensors to gather relevant information. The LiDAR detection area is a circular area centered on the center of mass of the FMR and the radius of LiDAR radiation range is d_s, as shown in the blue line area in Fig. 4. The infrared sensor is located directly in front of the FMR, its detection area is approximately regarded as a fan-shaped detection area with the center of mass of the car as the center and ζ is the ultrasonic radiation angle, as displayed in the red line area in Fig. 4. As the FMR follows its original trajectory, the LiDAR detection system continuously monitors its surroundings. If an obstacle is detected that would collide with the original trajectory, then the system transitions into the obstacle avoidance mode. The infrared sensor is then activated to obtain information about the size of the obstacle by emitting infrared signals. The infrared ray angle at which obstacles are perceived is expressed as ς, which can characterize obstacle size.

3.2.2 Dynamic tracking strategy of sub-target points

To ensure the safe navigation of the FMR around obstacles and a seamless transition back to its original trajectory, a dynamic tracking strategy utilizing sub-target points is employed for the FMR's obstacle avoidance trajectory replanning. The design process, as illustrated in Fig. 5, is divided into two parts, namely, the design of a regional dynamic forward strategy and the design of an optimal path function.

a) Sub-target point regional dynamic forward strategy design

When the obstacle avoidance mode is activated, the system considers a specified area in front of the current position of the FMR on its original reference trajectory as the sub-target zone for the FMR's obstacle avoidance plan. As the FMR moves forward, the sub-target zone also moves ahead at a constant speed. Specifically, dynamic forward strategy of the sub-target point area center is designed as follows:

$$\begin{cases} S_{p_{\mathrm{sub}}}(t) = \Gamma V_1 t + d, \\ \Gamma = \tau \cos\psi(t), \\ d = \upsilon \sin\varsigma, \end{cases} \tag{38}$$

where τ is the yaw correction parameter, υ is the obstacle-size correction parameters, $\tau, \upsilon \in \mathbb{R}^+$, Γ is the dynamic adjustment factor for the moving of the sub-target point area, $\psi(t)$ is the angle between the heading of the mobile robot at each moment and the tangent direction of the sub-target point on the original trajectory,

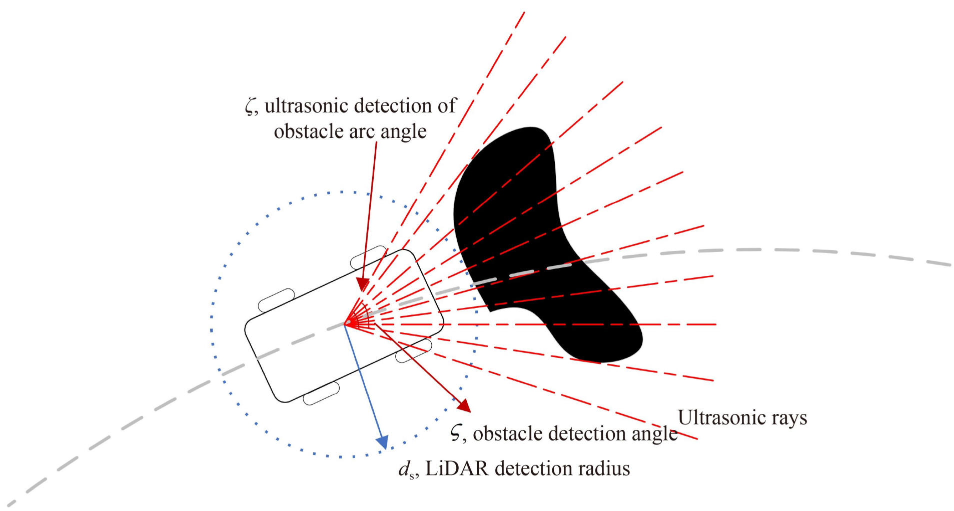

Fig. 4 Environmental interaction model of a four-wheeled mobile robot.

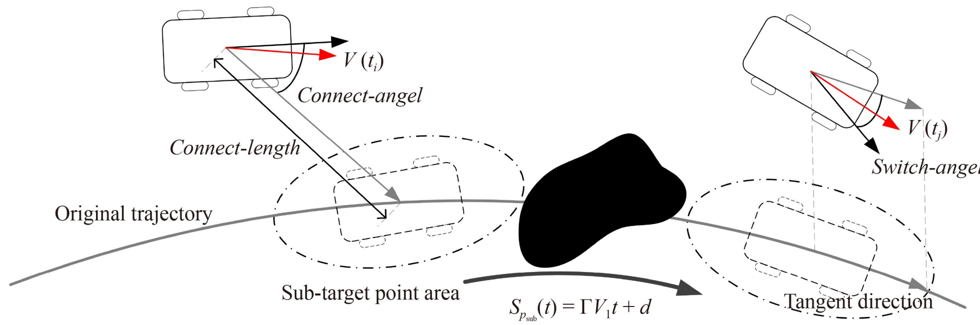

Fig. 5 Path optimization function criteria and sub-target point areas.

d is the initial distance of the sub-target point area related to the obstacle, and ς is the infrared angle of perceiving obstacles as mentioned in the above interactive model in Subsection 3.2.1.

The process of expanding from the center of the area to both sides to form the sub-target point area is expressed as follows:

$$\begin{cases} S_{p_{\text{sub1}}}(t) = \Gamma V_1 t + d - \kappa d, \\ S_{p_{\text{sub2}}}(t) = \Gamma V_1 t + d + \kappa d, \\ D(x) = \left\{ x \| x \in [S_{p_{\text{sub1}}}, S_{p_{\text{sub2}}}] \right\}, \end{cases} \tag{39}$$

where $S_{p_{\text{sub1}}}$ and $S_{p_{\text{sub2}}}$ denote the upper and lower bounds of the sub-target point area, respectively, $\kappa \in \mathbb{R}^+$, and $D(x)$ is the sub-target point area.

b) Path optimal function design

Once the sub-target area has been determined, the average sampling method is used to select a target point within the sub-target area, which is expressed as:

$$x_i = S_{p_{\text{sub}}}(t) \pm ic, \ i = 0, 1, ..., \left[\frac{\kappa}{i} \right], \tag{40}$$

where c is the sampling interval and x_i is the selected target point. At each moment, the trajectory planning to bypass obstacles is performed individually for the chosen sub-target points, resulting in multiple replanning paths with varying characteristics. To enhance the efficiency of the planning process, these replanning paths must be as short as possible. Furthermore, to minimize the oscillation of the system when returning to the original trajectory, the FMR is applied to retain the angle between the velocity direction and the tangent direction of the original trajectory as small as possible during the return. Therefore, this research selects the following factors as weight values to design the optimal objective function: 1) *Switch-angel*: the angle between the instantaneous velocity direction of the FMR and the tangent direction of the sub-target point on the original trajectory; 2) *Connect-angel*: the angle between the instantaneous velocity direction of the FMR and the direction in which the FMR connects to the sub-target point; and 3) *Connect-length*: the distance between the FMR and the sub-target point:

$$\begin{aligned} COST(i) = {} & \alpha \cdot Switch\text{-}angel(x_i, x_{\text{o}}) \\ & + \beta \cdot Connect\text{-}length(x_i, x_{\text{o}}) \\ & + \varpi \cdot Connect\text{-}angel(x_i, x_{\text{o}}), \end{aligned} \tag{41}$$

where x_{o} represents the current location of FMR, and α, β, and ϖ denote the adjustable parameter coefficients, which can be utilized to alter the requirements for the replanning path in accordance with the actual conditions.

3.2.3 Improved VFH+ local planning algorithm

An improved VFH+ planning algorithm is proposed for the local planning of the selected sub-target points and the current position of the FMR at a specific moment. First, a polar coordinate histogram is established with the FMR as the center. The angle and obstacle information of each cell in the polar coordinate histogram are represented as follows:

$$\begin{cases} \beta'_{i,j} = \arctan \dfrac{y - y^{\text{ob}}_{i,j}}{x - x^{\text{ob}}_{i,j}}, \\ m_{i,j} = C^2_{i,j} \left(a - b d^{\text{ob}}_{i,j}(q) \right), \end{cases} \tag{42}$$

where $\beta'_{i,j}$ is the angle from the center of the specific obstacle unit to the FMR in the world coordinate system, $m_{i,j}$ is the size of the obstacle vector at cell (i, j), $C_{i,j}$ is the obstacle determination value of the active cell, and a and b are normal parameters.

Considering that the FMR has a certain volume, each cell is expanded to prevent collisions. The density of polar obstacles after the expansion can be described as follows:

$$\begin{cases} k = \left[\dfrac{\beta'_{i,j}}{\alpha'} \right], \ \gamma_{i,j} = \arcsin \dfrac{d_{\text{r+s}}}{d^{\text{ob}}_{i,j}}, \ d_{\text{r+s}} = d_{\text{ero}} + d_{\text{s}}, \\ h'_{i,j} = \begin{cases} 1, \text{ if } k \cdot \alpha' \in \left[\beta'_{i,j} - \gamma_{i,j}, \beta'_{i,j} + \gamma_{i,j} \right], \\ 0, \end{cases} \\ H_{\text{func}} = \displaystyle\sum_{i,j} m_{i,j} \cdot h'_{i,j}, \end{cases} \tag{43}$$

where α' is the set angle resolution, k is the sector area number corresponding to the obstacle angle, $d_{\text{r+s}}$ is the radius of the obstacle unit after expansion, and H_{func} is the polar coordinate obstacle density function.

Due to the fact that the conventional VFH algorithm leads to fluctuations in the polar obstacle density around a fixed threshold, resulting in significant steering for the

FMR, which is inconsistent with its motion characteristics, a binarization design for the polar barrier density is proposed as follows:

$$H_{\text{func}}^{\text{B}} = \begin{cases} 1, \text{ if } H_{\text{func}} > \tau_{\text{h}}, \\ 0, \text{ if } H_{\text{func}} < \tau_{\text{l}}, \\ H_{\text{funclasttime}}^{\text{B}}, \text{ other}, \end{cases} \tag{44}$$

where $H_{\text{func}}^{\text{B}}$ denotes the polar coordinate obstacle density function after binarization processing, τ_{h} and τ_{l} are the set boundaries of binarization judgment, and $H_{\text{funclasttime}}^{\text{B}}$ is the polar coordinate obstacle density that corresponds to the last moment.

Based on the binarized polar coordinate obstacle density function, the forward direction of the FMR can be categorized into two situations, namely, narrow and wide valleys, which meet the condition $H_{\text{func}}^{\text{B}} = 0$. The fan-shaped valley k_{tar} that is most likely to be closest to the target point is selected among them. For the narrow valley, which indicates that the valley boundary range is less than k_{tar} plus the set maximum width (i.e., $k_{\text{bound}} < k_{\text{tar}} + s_{\max}$), the forward direction of the mobile robot is $\theta' = (k_{\text{tar}} + k_{\text{bound}})/2$. Meanwhile, for the wide valley, which indicates that the boundary range is greater than k_{tar} plus the set maximum width (i.e., $k_{\text{bound}} \geqslant k_{\text{tar}} + s_{\max}$), the forward direction of the FMR can be chosen as $\theta' = (2k_{\text{tar}} + s_{\max})/2$. This way, the reference angle for planning and the actual angle for tracking control can be obtained.

Remark 8. Sub-target areas and dynamic tracking are established to allow the FMR to return to the original trajectory after avoiding obstacles, thereby reducing computation and enhancing efficiency. The design of the sub-target point area can select the most appropriate movement direction, achieving efficient and smooth obstacle avoidance during the trajectory tracking process.

Remark 9. Considering the actual motion characteristics of the FMR, the strategy only considers a 90° turn in a single forward direction using the method of binarizing the polar obstacle density to avoid planning excessive or unreasonable turns with sharp angles. Additionally, the dynamic tracking process satisfies the requirement that the FMR moves closer to the original trajectory by adjusting the movement speed of sub-target points (i.e., $S_{p_{\text{sub}}}(t) = \Gamma V_1 t + d$). No trajectory phase difference would prevent the FMR from returning to the original trajectory.

4 Experiments and results

4.1 Experimental setup

The implementation of the trajectory tracking for the FMR is depicted in Fig. 6. The core FMR is equipped with various critical components, such as an industrial computer, LiDAR, electric cabinet, driving wheel, driving motor, steering motor, robot arm, and vision camera. The perception component, which consists of an induction LiDAR, ultrasonic sensor, and anti-collision strip, captures the state information of the FMR and transmits it to the industrial computer in the form of IO signals, digital pulses, velocities, and point clouds. Once the vehicle information is obtained, the control framework that has been downloaded into the industrial computer

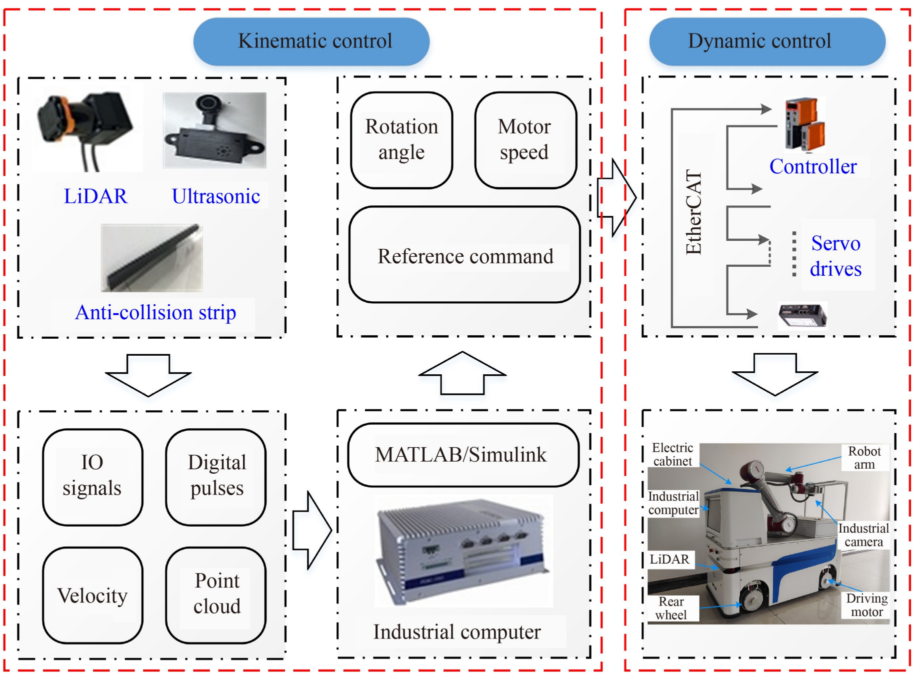

Fig. 6 Structure of the implementation of the four-wheeled mobile robot.

analyzes the data using MATLAB/Simulink and outputs the appropriate tracking strategy, including the rotation angle, motor speed, and updated reference command to the control module. Subsequently, the vehicle controller sends the control commands to the drive and steering motors to guide the FMR along the optimal trajectory. The performance and safety of the FMR can be monitored through the screen of the industrial computer to ensure optimal operation.

The controller in this experiment adopts a control distribution strategy, where the kinematic control of the upper layer and the dynamic control of the lower layer are combined, as shown in Fig. 6. The kinematic control layer is the control framework proposed in this study and has been verified through subsequent experiments. The dynamic control layer usually uses conventional PID control to transmit the angle control amount obtained from the kinematic control layer to the wheel servo motor accurately. Considering that the control process is redundant and focuses on stability, it is typically completed using an independent set of dynamic control theory, which will be studied in the future. Given that the parameters of the experimental platform for different methods are the same, the impact of the dynamic control layer on the tracking and obstacle avoidance of the mobile robot can be considered negligible.

For implementation, Fig. 7 illustrates the step-by-step process involved in the OCAC control, demonstrating the relationship between trajectory tracking and obstacle avoidance. Additionally, the parameters of ADTSMCAG are specified as $L_f = L_r = 0.445$ m, $\chi_1 = 10$, $\chi_2 = 1$, $\chi_3 = 0.26$, $\chi_4 = 0.22$, $\beta_1 = 0.5$, and $\beta_2 = 2.0$. The initial values of the hitting laws are determined as $h_1 = 6$, $h_2 = 1$, $h_3 = 1$, $m_0 = 0.5$, $m_1 = 1.5$, and $m_2 = 0.25$. A control sample time 0.1 ms is applied for the implementation of the developed FMR system. To highlight the advantages of the proposed ADTSMCAG method, we adopt the following methods for comparison: commonly-used benchmark PID controller ($k_p = 1.5$, $k_i = 0.6$, $k_d = 1.6$), common SMC (CSMC) ($q_1 = 1.8$, $q_2 = 1$), and ADTSMCAG derived by the proposed control principle.

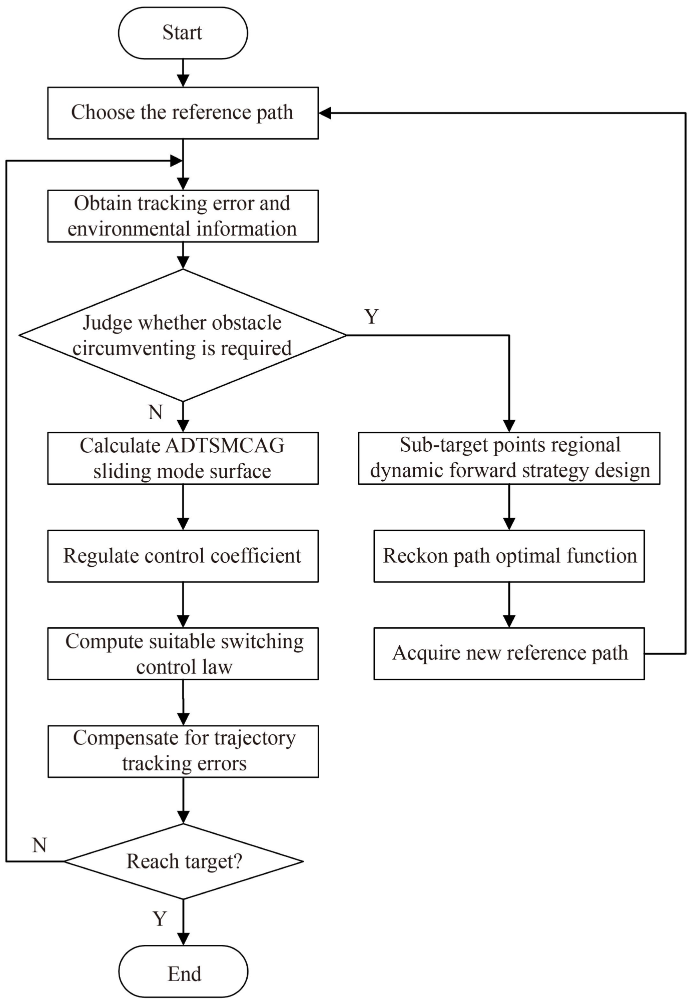

Fig. 7 Implementation procedure of the obstacle-circumventing adaptive control method. ADTSMCAG: anti-disturbance terminal slide mode control with adaptive gains.

4.2 Results and discussion

The testing procedure of the proposed FMR trajectory tracking scheme is demonstrated in a simplified scenario that consists of a combination of a straight-line path and two arc tracks, as shown in Fig. 8. The OCAC control framework is used as the vehicle controller strategy, which allows FMR to trace the designated trajectory accurately and efficiently. The tracking errors, including x_e, y_e, θ_e, and the sliding surface value s, are displayed in Fig. 9. The results show that the control sliding surface and tracking errors of FMR converge rapidly, demonstrating the strong robustness of the proposed control scheme. The adaptive robust performance of the proposed scheme is evaluated in three different working conditions, namely, Cases 1–3, hence further confirming the feasibility and effectiveness of the proposed protocol and FMR.

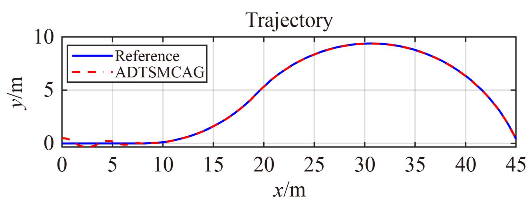

Fig. 8 Tracking responses under simplified condition. ADTSMCAG: anti-disturbance terminal slide mode control with adaptive gains.

Case 1. Tracking performance in non-vibration ground

In the first case, the ability of FMR to track a trajectory on a relatively ideal ground with minimal environmental vibrations was tested. The test results, as shown in Fig. 10, indicate that the proposed ADTSMCAG strategy can track the trajectory more quickly and accurately than the CSMC and PID control methods. The staged control approach of ADTSMCAG allows it to complete the trajectory tracking process in a faster and more stable manner compared with CSMC. As shown in Fig. 11, the sliding surface control process of ADTSMCAG converges to zero faster and has better stability once it reaches the sliding surface when the tracking trajectory encounters sharp turns. x_e, y_e, and θ_e tracking errors of FMR are shown in Figs. 12(a)–12(c), respectively, further highlighting the superiority of the ADTSMCAG control strategy.

Figure 12 displays the impressive performance of the proposed ADTSMCAG, with the initial tracking position error set at (0, 0.3, 0.5). The results demonstrate that x_e, y_e, and θ_e can converge quickly and stably to low levels. Fig. 12(c) provides a closer look at the angle error analysis of the FMR and shows that the proposed ADTSMCAG can effectively converge θ_e close to zero

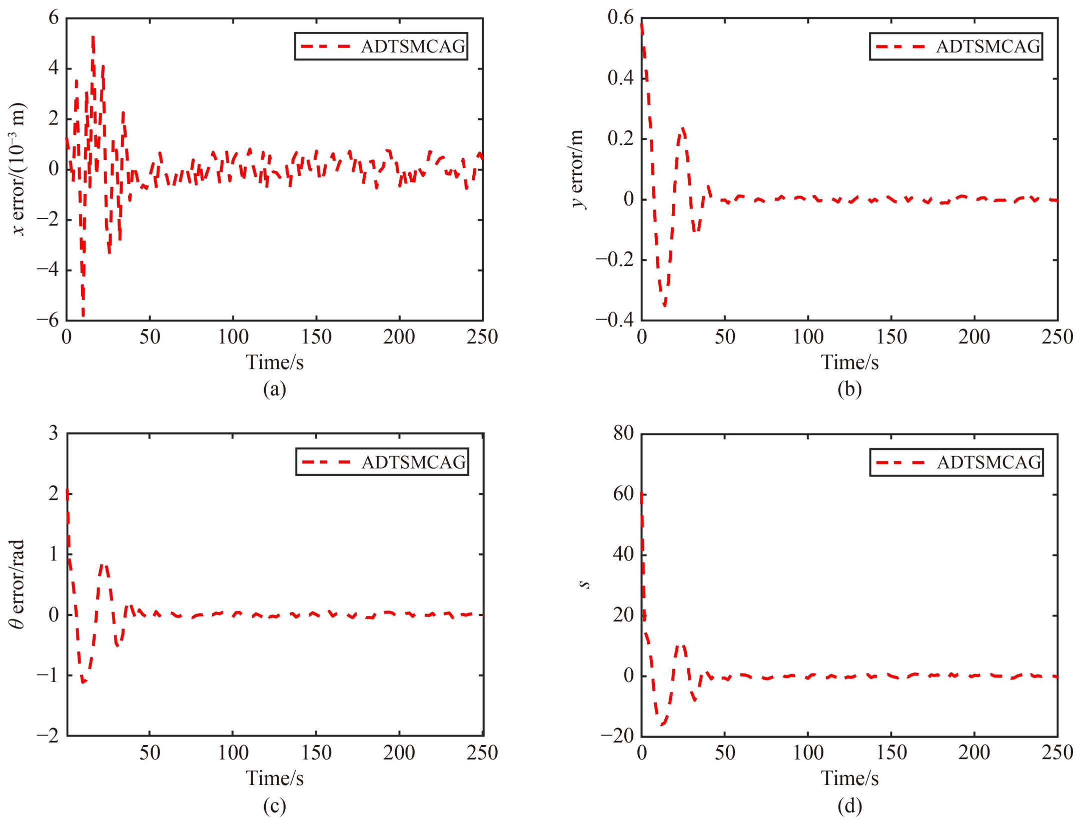

Fig. 9 Tracking errors and sliding surface under simplified condition: (a) value of x error, (b) value of y error, (c) value of θ error, and (d) value of s. ADTSMCAG: anti-disturbance terminal slide mode control with adaptive gains.

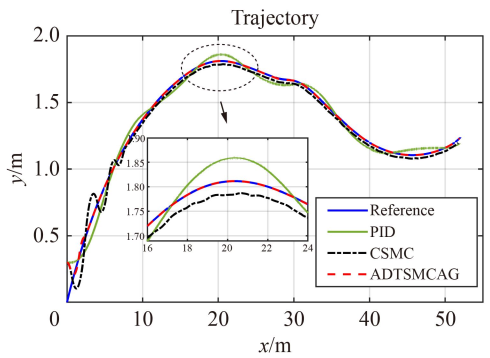

Fig. 10 Tracking responses of Case 1. ADTSMCAG: anti-disturbance terminal slide mode control with adaptive gains, CSMC: common slide mode control, PID: proportional−integral−derivative.

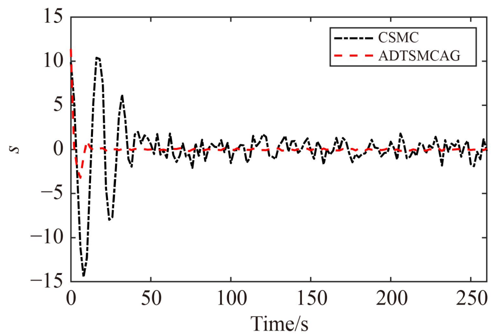

Fig. 11 Sliding surfaces of Case 1. CSMC: common slide mode control, ADTSMCAG: anti-disturbance terminal slide mode control with adaptive gains.

within a limited time with only small fluctuations. Furthermore, the CSMC control method is plagued by jitters during the initial stage of convergence, accompanied by significant fluctuations in the steady-state process. Figure 12(a) emphasizes that the proposed ADTSMCAG ensures x_e to converge to a low level consistently during the tracking process. Notably, Fig. 12(b) demonstrates the exceptional performance of ADTSMCAG, with quick convergence of y_e to zero and improved stability during the trajectory tracking control through θ, which directly affects the overall trajectory tracking effect, as observed in Fig. 10. To present a clear picture of the tracking effect of ADTSMCAG, Fig. 13 depicts a violin diagram analysis of the errors of x_e, y_e, and θ_e. The results indicate that ADTSMCAG has a closer convergence to zero and fewer outliers than the CSMC and PID control methods in the three datasets.

Case 2. Tracking performance with vibration noise

In the presence of environmental vibration, the actual working scenario of FMR can result in unpredictable errors in the trajectory tracking process. To test this scenario, a reference trajectory was selected for comparison with the proposed ADTSMCAG, CSMC, and PID control methods. The results, as shown in Fig. 14, indicate that the proposed ADTSMCAG control method

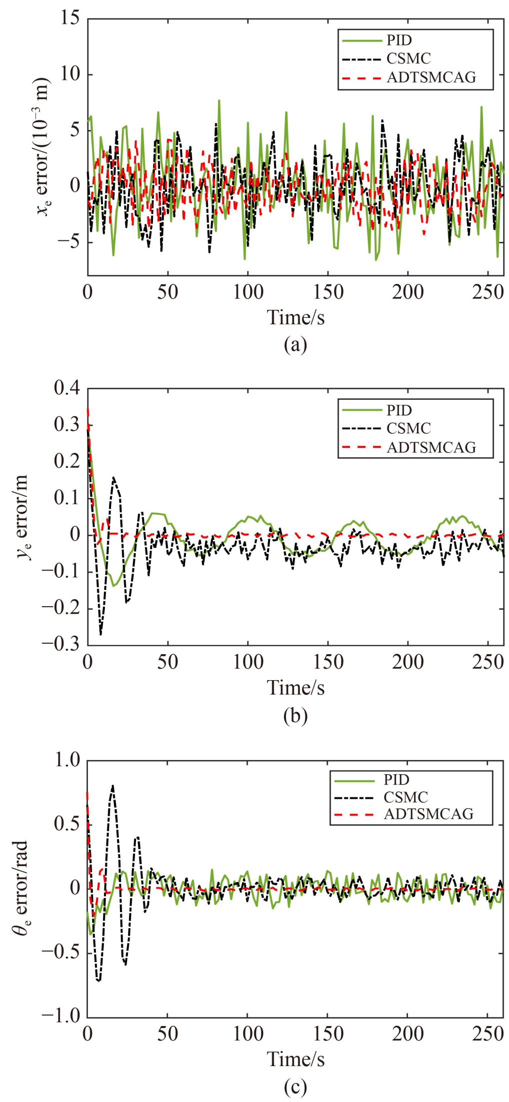

Fig. 12 Tracking errors of Case 1: (a) errors of x_e, (b) errors of y_e, and (c) errors of θ_e. ADTSMCAG: anti-disturbance terminal slide mode control with adaptive gains, CSMC: common slide mode control, PID: proportional−integral−derivative.

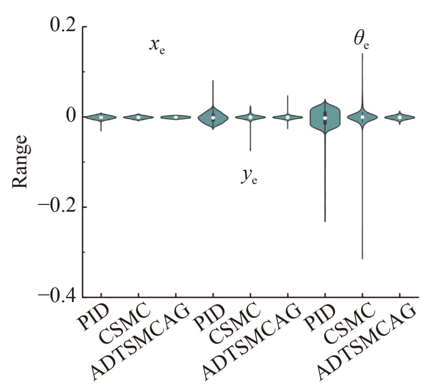

Fig. 13 Tracking error statistics of Case 1. ADTSMCAG: anti-disturbance terminal slide mode control with adaptive gains, CSMC: common slide mode control, PID: proportional−integral−derivative.

smoothly guides the FMR along the reference path, with minimal oscillations, demonstrating the robustness of the method. In contrast, both CSMC and PID control display significant oscillations, with CSMC showing excessive chattering during the early stages of convergence and PID having a relatively long tracking and regression time. The sliding mode surface convergence process of ADTSMCAG and CSMC is depicted in Fig. 15.

Furthermore, the proposed ADTSMCAG exhibits superior tracking accuracy compared with PID and CSMC (Fig. 16). In this case, the starting error is set to (0, 1, 0.5). The convergence θ_e of the control object can be seen in Fig. 16(c), where ADTSMCAG converges quickly when it is far from the sliding surface and slows down as it approaches the surface to maintain stability. In contrast, CSMC experiences significant oscillations far from the sliding surface, leading to low convergence efficiency. Meanwhile, PID's performance in maintaining a steady state after reaching the sliding surface is less satisfactory. x_e and y_e are displayed in Figs. 16(a) and 16(b), respectively. To provide a clear visualization of the tracking performance, a violin plot that illustrates the errors in the three datasets is presented in Fig. 17. The errors produced by ADTSMCAG are more concentrated within a small range compared with PID and CSMC.

Case 3. Obstacle avoidance performance

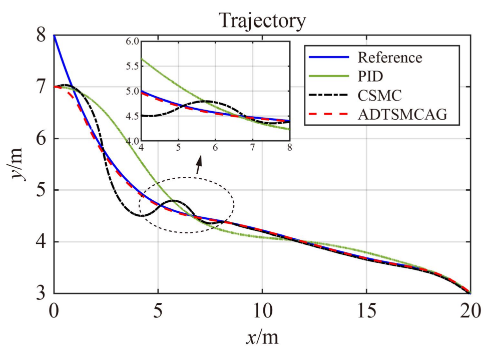

Fig. 14 Tracking responses of Case 2. ADTSMCAG: anti-disturbance terminal slide mode control with adaptive gains, CSMC: common slide mode control, PID: proportional−integral−derivative.

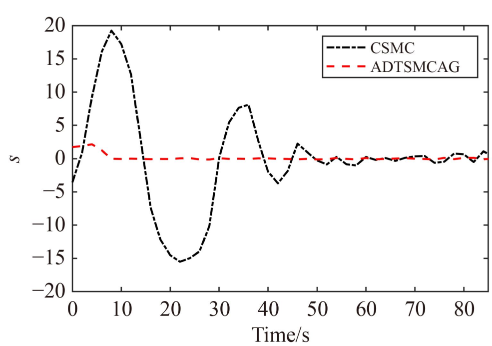

Fig. 15 Sliding surfaces of Case 2. CSMC: common slide mode control, ADTSMCAG: anti-disturbance terminal slide mode control with adaptive gains.

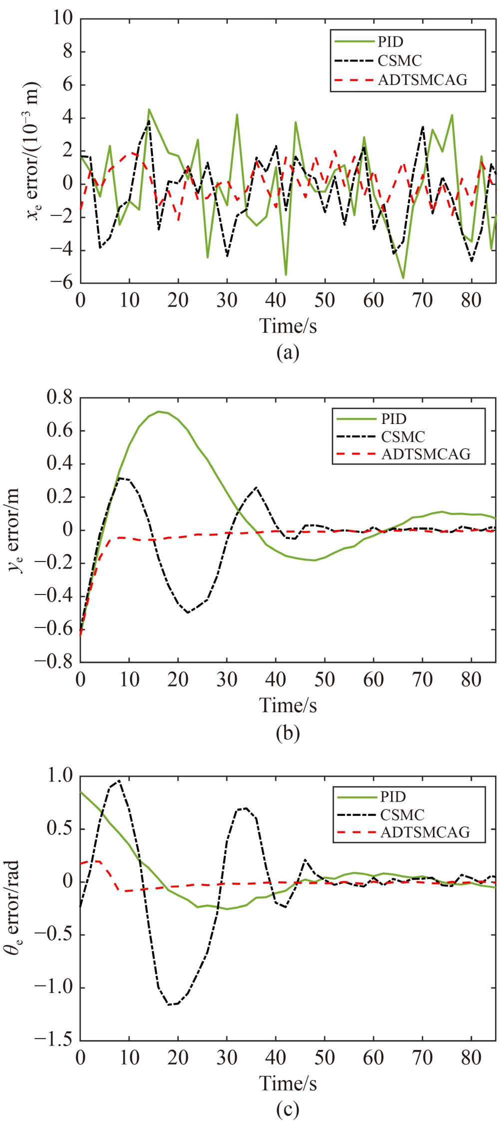

Fig. 16 Tracking errors of Case 2: (a) errors of x_e, (b) errors of y_e, and (c) errors of θ_e. CSMC: common slide mode control, ADTSMCAG: anti-disturbance terminal slide mode control with adaptive gains, PID: proportional−integral−derivative.

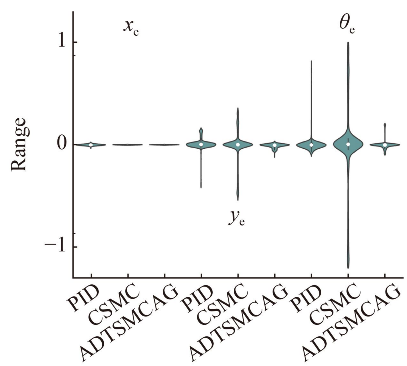

Fig. 17 Tracking error statistics of Case 2. ADTSMCAG: anti-disturbance terminal slide mode control with adaptive gains, CSMC: common slide mode control, PID: proportional−integral−derivative.

A scenario with unknown obstacles on the reference trajectory was selected to verify the obstacle avoidance capabilities of the SDTROA strategy. This scenario would demonstrate the quality of the replanned paths that resulted from the obstacles detected in the environment and would allow for a comparison between the proposed SDTROA strategy and a traditional APF (TAPF) obstacle avoidance local planning algorithm [33]. Subsequently, the simulation and experimental results would verify the superiority of the SDTROA strategy.

During the simulation test, the starting and ending points were set to (50, 180) and (100, 40), respectively. The original trajectory was formulated considering the original obstacle distribution of the map, as shown in Fig. 18, which incorporates a path softening procedure. The FMR was assumed to follow the original trajectory when no obstacles were detected during the trajectory tracking process. Notably, the trajectory tracking error was not considered in the obstacle avoidance experiment.

To test the trajectory tracking ability of FMR, artificial obstacles are set along the original trajectory. As depicted in Fig. 18, a dynamic obstacle is depicted as a black circle with a radius of 2.5 pixels. The detection range of the FMR is defined as a circular area centered on its current position, with a radius of 50 pixels. Whenever the FMR detects an obstacle, a safety distance of 2.5 pixels is established to ensure the safety of its trajectory, as demonstrated by the black area in Fig. 18.

As shown in Fig. 19, when FMR encounters an obstacle, it replans its path by using the dynamic sub-target point as the new endpoint for obstacle avoidance. The actual path taken by the FMR, using the SDTROA method to replan the original trajectory, is represented by the red curve in the figure. In contrast, the green curve represents the comparison of the TAPF obstacle avoidance path planning. Figure 19(a) illustrates a scenario with a few obstacles present on the original path, while Fig. 19(b) displays the effectiveness of FMR's obstacle avoidance and replanning when numerous dynamic obstacles are present. In comparison with the TAPF obstacle avoidance method, the proposed SDTROA strategy enables a faster return to the original path and a higher level of alignment with the original trajectory, thereby enhancing the efficiency of planning and tracking.

The results presented in Table 1 indicate that the SDTROA tracking process yields a trajectory that exhibits a closer alignment and a higher level of coincidence with the original path, regardless of the number of obstacles. As depicted in Fig. 20, the

Fig. 18 Obstacles on the original trajectory.

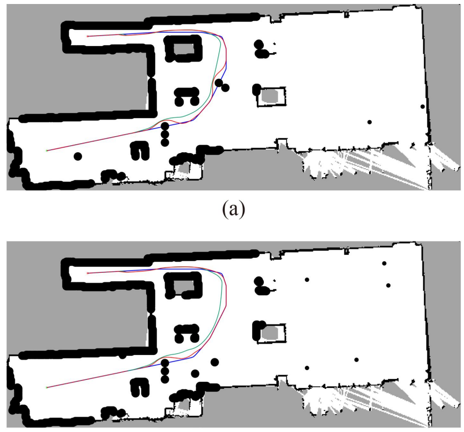

(a)

(b)

Fig. 19 Dynamic obstacle avoidance simulation test using sub-target dynamic tracking regression obstacle avoidance strategy: (a) trajectory with few dynamic obstacles and (b) trajectory with more dynamic obstacles.

Table 1 Trajectory re-planning performance

Obstacles	Strategy	Coincidence degree	Planning time/s
Few dynamic obstacles	TAPF	0.225	16.2
	SDTROA	0.681	10.8
More dynamic obstacles	TAPF	0.194	25.3
	SDTROA	0.575	12.4

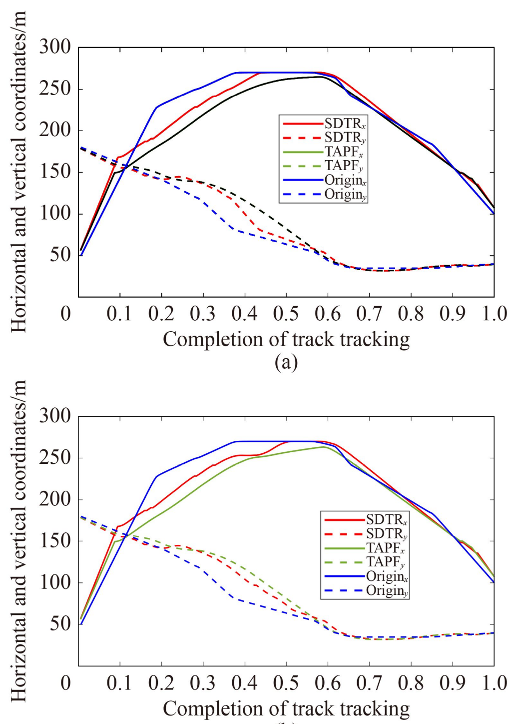

(a)

(b)

Fig. 20 States of the four-wheeled mobile robot when avoiding the obstacles: (a) trajectory with few dynamic obstacles and (b) trajectory with more dynamic obstacles.

SDTROA strategy consistently stays near the original trajectory at each moment, demonstrating its superior performance compared with the TAPF obstacle avoidance method. Additionally, the SDTROA method is also efficient, with a short full planning time, as reflected in Table 1.

In our tracking test, we selected a scene with multiple obstacles to demonstrate the performance of our control frameworks. As shown in Fig. 21(a), we employed two control frameworks for obstacle avoidance tracking control, namely, the SDTROA (OCAC) framework and the TAPF framework, both of which utilize the

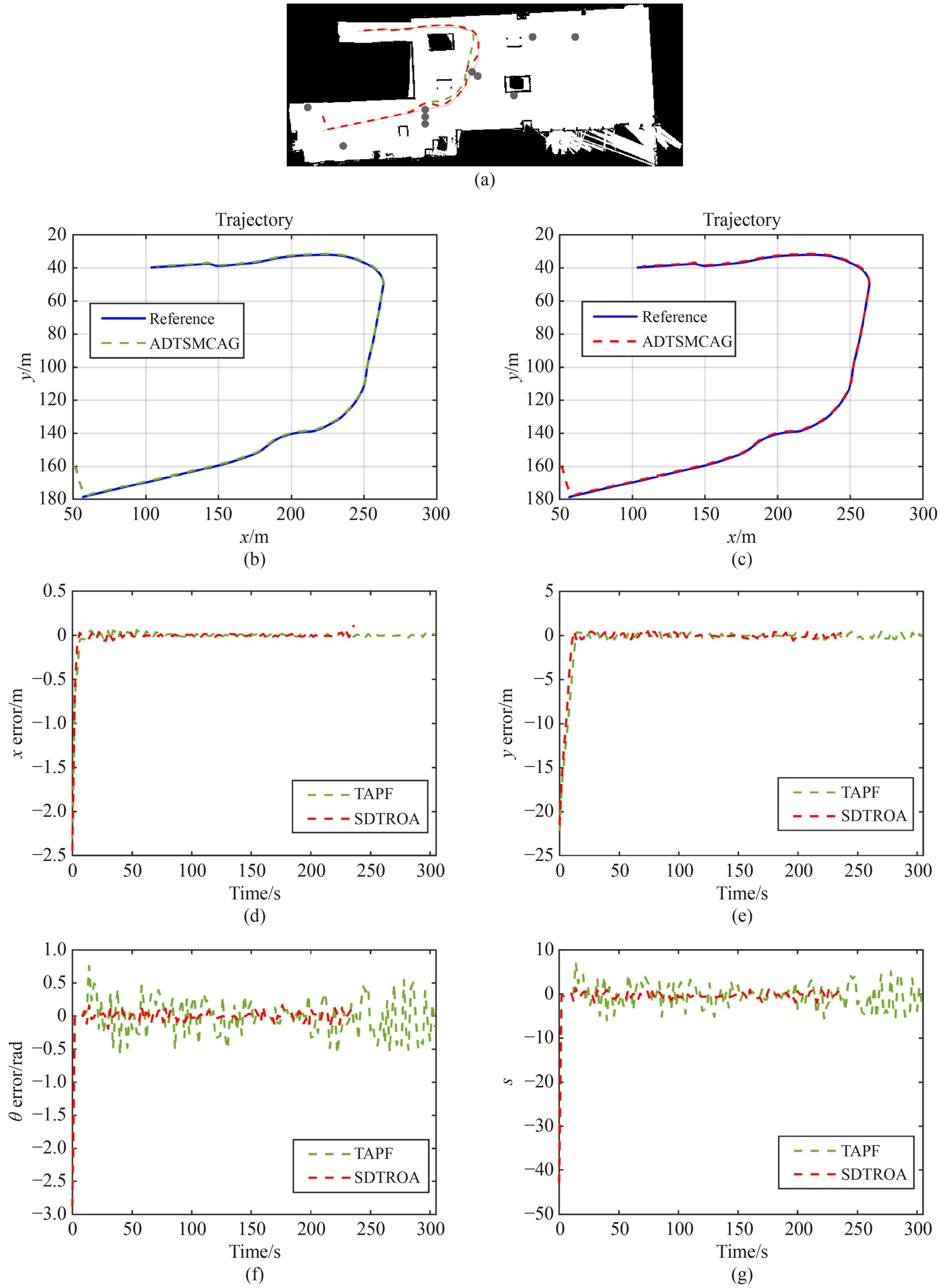

Fig. 21 (a) Dynamic obstacle avoidance tracking experiment: tracking using traditional artificial potential field (TAPF) and sub-target dynamic tracking regression obstacle avoidance (SDTROA); (b) tracking using TAPF; (c) tracking using SDTROA; (d) value of x error; (e) value of y error; (f) value of θ error; and (g) value of s.

ADTSMCAG tracking method. The comparison of the x_e, y_e, θ_e, and sliding mode surface can be observed in Fig. 21(b). When comparing the TAPF control framework with the OCAC framework, we found that the latter effectively utilized the original optimal path more effectively, resulting in a shorter tracking time and higher efficiency. Furthermore, due to the high level of coordination between planning and control, the tracking process under the OCAC framework exhibited remarkable stability and robustness.

5 Discussion and extensions

1) The proposed method is not only suitable for the limited time control of FMR but can also be applied to many commonly used angle-driven mobile robot systems. This paper adopts a unique allocation control model, incorporating kinematic and dynamic controls, with emphasis on the former for the high-precision and rapid control of the system. In contrast to many models that solely rely on dynamic control [43–45], this approach has the advantage of incorporating kinematic and dynamic control layers. Many existing studies [46–48] that analyze the trajectory tracking control accuracy of mobile robots or other systems also highlight this combination. Additionally, PID control is still the most commonly used technique for the dynamic control of mobile robots or other systems [49,50] to maintain system stability and reduce the likelihood of operating failure.

2) The presence of the sign term in SMC ensures that the system converges to the sliding surface. Its gain accelerates the convergence speed of the system. However, the high-frequency switching feature brought by the sign term leads to severe oscillation in the system. This paper adopts fuzzy logic to adjust control gains h_1 and h_2 moderately, ensuring that the system minimizes oscillation while satisfying the condition of finite-time convergence. Many existing studies [51–53] also used fuzzy logic to eliminate chattering in sliding mode systems. In addition to the use of fuzzy logic, the use of boundary layer methods [54] can also be considered when eliminating chattering in sliding mode systems, such as replacing the sign function with *sat* and tanh. Some combination of traditional terms [55] can also be used to eliminate chattering in sliding mode systems.

3) The proposed obstacle avoidance algorithm in this paper is specifically designed to determine the characteristics of the presented FMR. Unlike traditional omni-wheels, such as Mecanum wheel [56], the common movement modes of the proposed FMR include modes, such as translational, Ackermann, and variable Ackermann, which cannot achieve a large directional turning angle of 180°. To address this feature, when designing the local obstacle avoidance strategy for FMR, direction constraints should be added when using the VFH+ obstacle avoidance method to avoid frequent direction changes [57]. Additionally, the trajectory tracking model established in this paper is based on the variable Ackermann model, which significantly differs from the common differential and steer wheel models. Thus, the use of a new trajectory tracking control method design is necessary. Therefore, new trajectory tracking control and obstacle avoidance strategy designs are essential.

6 Conclusions

This study presents a new framework for OCAC. The proposed framework consists of a novel ADTSMCAG method and a new SDTROA strategy. The ADTSMCAG method is designed to provide rapid convergence and final stability by utilizing a modified proportional−integral sliding mode surface and a phased approach control law. The SDTROA strategy transforms the traditional obstacle avoidance planning into a dynamic target-tracking problem by proposing a new dynamic tracking strategy for sub-target points. Efficient and smooth obstacle avoidance in the trajectory tracking process can be achieved when combined with the improved VFH+ local planning algorithm. The communication between the trajectory tracking and replanning obstacle avoidance strategies is achieved by controlling actual and reference states, resulting in the complete tracking of the system. The proposed framework has been verified through experiments under various motion conditions. With the introduction of ADTSMCAG, the efficiency and robustness of tracking control in complex industrial scenarios with potential obstacles have been improved. This new control law outperforms traditional tracking control methods, partly due to the integration of a dynamic target point obstacle avoidance strategy. The coupling of these two components enhances the efficiency of the FMR system and results in improved tracking performance compared with asynchronous methods.

In future research, the trajectory tracking control of the FMR is expected to be integrated with the study of perception systems to improve its real-time accuracy and obstacle avoidance regression efficiency. Potentially, by incorporating a more sensitive perception system, the trajectory tracking performance and obstacle avoidance capabilities of FMR can be enhanced.

Nomenclature

Abbreviations

ADTSMCAG Anti-disturbance terminal slide mode control with adaptive gain

APF	Artificial potential field
CSMC	Common slide mode control
ESO	Extended state observer
FMR	Four-wheeled mobile robot
FTC	Fault-tolerant controller
MPC	Model predictive control
OCAC	Obstacle-circumventing adaptive control
PID	Proportional−integral−derivative
RBF	Radial basis function
RCM	Remote center of movement
SDTROA	Sub-target dynamic tracking regression obstacle avoidance
SMC	Slide mode control
TAPF	Traditional artificial potential field
VFH	Vector field histogram
VFH+	Vector field histogram+

Variables

a, b	Normal numbers
$A^i_{s\dot{s}}$	Fuzzy set of system input
$B^i_{h_1}$, $B^i_{h_2}$	Fuzzy sets of system output
c	Sampling interval
$C_{i,j}$	Obstacle determination value of the active cell
$COST(i)$	Optimal objective function
d	Initial increment of the sub-target point area related to the obstacle
d_{ero}	Corrosion radius of the obstacle unit after considering the safety distance
$d^{\mathrm{ob}}_{i,j}(\boldsymbol{q})$	Distance from the current position of FMR to the center of the obstacle unit
$d_{\mathrm{r+s}}$	Radius of the obstacle unit after expansion
d_{s}	Radius of the radar scanning area
$D(x)$	Sub-target point area
g, λ	Positive parameters satisfying $g > 2$ and even
$G^{\mathrm{ob}}_{i,j}(\boldsymbol{q})$	Obstacle avoidance constraints
h_1, h_2, h_3	Preset control gains satisfying: $h_1 > \gamma\chi_1 \cdot \mathrm{sign}(S)/\lvert S\rvert^q$, $h_2 > 0$, and $h_3 > 0$
$h'_{i,j}$	Sub polar coordinate obstacle density function
H_k	Polar coordinate obstacle density function
$H^{\mathrm{B}}_{\mathrm{func}}$	Polar coordinate obstacle density function after binarization processing
$H^{\mathrm{B}}_{\mathrm{funclasttime}}$	Polar coordinate obstacle density corresponding to the last moment
i	Selected target point label
k	Sector area number corresponding to the obstacle angle
k_{bound}	Boundary range
k_{tar}	Fan-shaped valley
L_{f}, L_{r}	Distances from front and rear wheels to the robot center, respectively
m_0, m_1, m_2	Positive parameters
$m_{i,j}$	Size of the obstacle vector at cell (i, j)
q_1, q_2	Positive parameters
$\boldsymbol{q}$, $\boldsymbol{q}_{\mathrm{rob}}$, $\boldsymbol{q}_{\mathrm{r}}$	Robot state, new reference trajectory state, and reference trajectory state, respectively
s	Sliding surface value
$s_{\max}$	Set maximum width
$S_{p_{\mathrm{sub}}}(t)$	Sub-target point area
$S_{p_{\mathrm{sub1}}}$, $S_{p_{\mathrm{sub2}}}$	Upper and lower bounds of the sub-target point area
$\dot{S}$	Adaptive sliding mode surface derivative
$S(t_n)$, $\bar{S}(t_n)$	Adaptive sliding mode surface and sub adaptive sliding mode surface, respectively
t	System convergence time
t_1, t_2	Time of phases 1 and 2, respectively
t_n	Control framework running time
t_{reach}	Time for the system to reach the sliding surface
T	Extending reference position
$T_{\max}$	Maximum convergence time
$\nu_{B^i_{h_1}}$, $\nu_{B^i_{h_2}}$	Membership degrees of the conclusion
V	Lyapunov function
V_{l}, V_{lr}	Linear velocity and reference linear velocity, respectively
x, y, θ	Robot positions
$\dot{x}$, $\dot{y}$, $\dot{\theta}$	Robot position derivatives
x_{e}, y_{e}, θ_{e}	Robot position errors
x_i	Selected target point
$x^{\mathrm{ob}}_{i,j}$, $y^{\mathrm{ob}}_{i,j}$	Coordinates of the obstacle unit
x_{o}	Current location of FMR
x_{r}, y_{r}, θ_{r}	Reference robot positions
$\dot{x}_{\mathrm{r}}$, $\dot{y}_{\mathrm{r}}$, $\dot{\theta}_{\mathrm{r}}$	Reference robot position derivatives
x_T, y_T	Position T
X_1, X_2	Variables of the equations of state
α, β, ϖ	Positive parameters
α'	Set angle resolution
β_1, β_2	Predefined error coefficients satisfying: $\beta_1 \in (1, \infty)$ and $\beta_2 \in (0, 1)$
$\beta'_{i,j}$	Angle from the center of the specific obstacle unit to the FMR
γ, γ'	Bounded lumped uncertainties and external disturbances, respectively
$\gamma_{i,j}$	Preset angle
$\varpi_{A^i_{s\dot{s}}}$	Membership degrees of the premise
δ_{f}, δ_{r}	Virtual front and rear wheel angles, respectively
θ'	Forward direction of FMR
θ_{obr}	Updated reference trajectory output
θ_P	Tangent direction angle of the reference position

$\chi_1, \chi_2, \chi_3, \chi_4$	Preset control gains
κ	Positive parameter
ς	Obstacle detection angle
ζ	Ultrasonic radiation angle
τ	Yaw correction parameter
τ_h, τ_l	Set boundaries of binarization judgment
Γ	Dynamic adjustment factor
υ	Obstacle-size correction parameter
$\psi(t)$	Angle between the heading of the FMR
Δ_t	System parameter perturbations
Ξ, Ω	Intermediate control variables

Acknowledgements The work was supported in part by the National Natural Science Foundation of China (Grant Nos. 52275488 and 52105019), in part by the Key R&D Program of Hubei Province, China (Grant No. 2022BAA064), and in part by Dongguan Social Development Project, China (Grant No. 20211800904902).

Conflict of Interest The authors declare that they have no conflict of interest.

References

1. Baumann D, Mager F, Wetzker U, Thiele L, Zimmerling M, Trimpe S. Wireless control for smart manufacturing: recent approaches and open challenges. Proceedings of the IEEE, 2021, 109(4): 441–467
2. Meng J, Wang S T, Li G, Jiang L Q, Zhang X L, Liu C, Xie Y L. Iterative-learning error compensation for autonomous parking of mobile manipulator in harsh industrial environment. Robotics and Computer-integrated Manufacturing, 2021, 68: 102077
3. Guo S, Jin Y, Bao S, Xi F F. Accuracy analysis of omnidirectional mobile manipulator with mecanum wheels. Advances in Manufacturing, 2016, 4(4): 363–370
4. Zhang X L, Zhang W X, Zhao Y Q, Wang H, Lin F, Cai Y F. Personalized motion planning and tracking control for autonomous vehicles obstacle avoidance. IEEE Transactions on Vehicular Technology, 2022, 71(5): 4733–4747
5. Xie Y L, Zhang X L, Meng W, Zheng S Q, Jiang L Q, Meng J, Wang S T. Coupled fractional-order sliding mode control and obstacle avoidance of a four-wheeled steerable mobile robot. ISA Transactions, 2021, 108: 282–294
6. Jiang L Q, Wang S T, Xie Y L, Xie S Q, Zheng S Q, Meng J, Ding H. Decoupled fractional supertwisting stabilization of interconnected mobile robot under harsh terrain conditions. IEEE Transactions on Industrial Electronics, 2022, 69(8): 8178–8189
7. Zheng K S, Wu F, Chen X P. Laser-based people detection and obstacle avoidance for a hospital transport robot. Sensors, 2021, 21(3): 961
8. Yu X, Jiang J. A survey of fault-tolerant controllers based on safety-related issues. Annual Reviews in Control, 2015, 39: 46–57
9. Singh A S P, Osamu N. Trajectory tracking and integrated chassis control for obstacle avoidance with minimum jerk. IEEE Transactions on Intelligent Transportation Systems, 2022, 23(5): 4625–4641
10. Xiao Z X, Hu M H, Fu C Y, Qin D T. Model predictive trajectory tracking control of unmanned vehicles based on radial basis function neural network optimisation. Proceedings of the Institution of Mechanical Engineers, Part D: Journal of Automobile Engineering, 2023, 237(2–3): 347–361
11. Khan A H, Li S, Luo X. Obstacle avoidance and tracking control of redundant robotic manipulator: an RNN-based metaheuristic approach. IEEE Transactions on Industrial Informatics, 2020, 16(7): 4670–4680
12. Xie Y L, Zhang X L, Zheng S Q, Ahn C K, Wang S T. Asynchronous H_∞ continuous stabilization of mode-dependent switched mobile robot. IEEE Transactions on Systems, Man, and Cybernetics. Systems, 2022, 52(11): 6906–6920
13. Yogi S C, Tripathi V K, Behera L. Adaptive integral sliding mode control using fully connected recurrent neural network for position and attitude control of quadrotor. IEEE Transactions on Neural Networks and Learning Systems, 2021, 32(12): 5595–5609
14. Ren C, Li X H, Yang X B, Ma S G. Extended state observer-based sliding mode control of an omnidirectional mobile robot with friction compensation. IEEE Transactions on Industrial Electronics, 2019, 66(12): 9480–9489
15. Azzabi A, Nouri K. Design of a robust tracking controller for a nonholonomic mobile robot based on sliding mode with adaptive gain. International Journal of Advanced Robotic Systems, 2021, 18(1): 1729881420987082
16. Huang J, Zhang M S, Ri S, Xiong C H, Li Z J, Kang Y. High-order disturbance-observer-based sliding mode control for mobile wheeled inverted pendulum systems. IEEE Transactions on Industrial Electronics, 2020, 67(3): 2030–2041
17. Dian S Y, Fang H W, Zhao T, Wu Q, Hu Y, Guo R, Li S C. Modeling and trajectory tracking control for magnetic wheeled mobile robots based on improved dual-heuristic dynamic programming. IEEE Transactions on Industrial Informatics, 2021, 17(2): 1470–1482
18. Chen Z Y, Liu Y, He W, Qiao H, Ji H B. Adaptive-neural-network-based trajectory tracking control for a nonholonomic wheeled mobile robot with velocity constraints. IEEE Transactions on Industrial Electronics, 2021, 68(6): 5057–5067
19. Zhang X L, Xie Y L, Jiang L Q, Li G, Meng J, Huang Y. Fault-tolerant dynamic control of a four-wheel redundantly-actuated mobile robot. IEEE Access: Practical Innovations, Open Solutions, 2019, 7: 157909–157921
20. Thomas M, Bandyopadhyay B, Vachhani L. Discrete-time sliding mode control design for unicycle robot with bounded inputs. IEEE Transactions on Circuits and Systems II: Express Briefs, 2021, 68(8): 2912–2916
21. Chen M. Robust tracking control for self-balancing mobile robots using disturbance observer. IEEE/CAA Journal of Automatica Sinica, 2017, 4(3): 458–465
22. Wang P W, Gao S, Li L, Cheng S, Zhao L. Automatic steering control strategy for unmanned vehicles based on robust backstepping sliding mode control theory. IEEE Access: Practical Innovations, Open Solutions, 2019, 7: 64984–64992
23. Zhao Y K, Zhang F, Huang P F, Liu X Y. Impulsive super-twisting

sliding mode control for space debris capturing via tethered space net robot. IEEE Transactions on Industrial Electronics, 2020, 67(8): 6874–6882

24. Norsahperi N M H, Danapalasingam K A. An improved optimal integral sliding mode control for uncertain robotic manipulators with reduced tracking error, chattering, and energy consumption. Mechanical Systems and Signal Processing, 2020, 142: 106747
25. Shi Z, Deng C C, Zhang S, Xie Y, Cui H T, Hao Y. Hyperbolic tangent function-based finite-time sliding mode control for spacecraft rendezvous maneuver without chattering. IEEE Access: Practical Innovations, Open Solutions, 2020, 8: 60838–60849
26. Sepestanaki M A, Barhaghtalab M H, Mobayen S, Jalilvand A, Fekih A, Skruch P. Chattering-free terminal sliding mode control based on adaptive barrier function for chaotic systems with unknown uncertainties. IEEE Access: Practical Innovations, Open Solutions, 2022, 10: 103469–103484
27. Alinaghi Hosseinabadi P, Ordys A, Soltani Sharif Abadi A, Mekhilef S, Pota H R. State and disturbance observers-based chattering-free fixed-time sliding mode control for a class of high-order nonlinear systems. Advanced Control for Applications: Engineering and Industrial Systems, 2021, 3(3): e81
28. Zhang W, Cheng H T, Hao L, Li X C, Liu M F, Gao X F. An obstacle avoidance algorithm for robot manipulators based on decision-making force. Robotics and Computer-integrated Manufacturing, 2021, 71: 102114
29. Huang Y J, Ding H T, Zhang Y B, Wang H, Cao D P, Xu N, Hu C. A motion planning and tracking framework for autonomous vehicles based on artificial potential field elaborated resistance network approach. IEEE Transactions on Industrial Electronics, 2020, 67(2): 1376–1386
30. Babinec A, Duchoň F, Dekan M, Mikulová Z, Jurišica L. Vector field histogram* with look-ahead tree extension dependent on time variable environment. Transactions of the Institute of Measurement and Control, 2018, 40(4): 1250–1264
31. Lee D H, Lee S S, Ahn C K, Shi P, Lim C C. Finite distribution estimation-based dynamic window approach to reliable obstacle avoidance of mobile robot. IEEE Transactions on Industrial Electronics, 2021, 68(10): 9998–10006
32. Guo K L, Su H, Yang C G. A small opening workspace control strategy for redundant manipulator based on RCM method. IEEE Transactions on Control Systems Technology, 2022, 30(6): 2717–2725
33. Upadhyay S, Ratnoo A. Continuous-curvature path planning with obstacle avoidance using four parameter logistic curves. IEEE Robotics and Automation Letters, 2016, 1(2): 609–616
34. Latombe J C. Robot motion planning. New York: Springer Science & Business Media, 2012
35. Lu Q, Zhang D, Ye W J, Fan J Y, Liu S, Su C Y. Targeting posture control with dynamic obstacle avoidance of constrained uncertain wheeled mobile robots including unknown skidding and slipping. IEEE Transactions on Systems, Man, and Cybernetics: Systems, 2021, 51(11): 6650–6659
36. Zhou X B, Yu X, Zhang Y M, Luo Y Y, Peng X Y. Trajectory planning and tracking strategy applied to an unmanned ground vehicle in the presence of obstacles. IEEE Transactions on Automation Science and Engineering, 2021, 18(4): 1575–1589
37. Chen H, Zhang X. Path planning for intelligent vehicle collision avoidance of dynamic pedestrian using Att-LSTM, MSFM and MPC at un-signalized crosswalk. IEEE Transactions on Industrial Electronics, 2022, 69(4): 4285–4295
38. Zhang Z J, Yang S, Chen S Y, Luo Y M, Yang H, Liu Y. A vector-based constrained obstacle avoidance scheme for wheeled mobile redundant robot manipulator. IEEE Transactions on Cognitive and Developmental Systems, 2021, 13(3): 465–474
39. He S D, Dai S L, Luo F. Asymptotic trajectory tracking control with guaranteed transient behavior for MSV with uncertain dynamics and external disturbances. IEEE Transactions on Industrial Electronics, 2019, 66(5): 3712–3720
40. Yang C G, Huang D Y, He W, Cheng L. Neural control of robot manipulators with trajectory tracking constraints and input saturation. IEEE Transactions on Neural Networks and Learning Systems, 2021, 32(9): 4231–4242
41. Liu C X, Wen G L, Zhao Z J, Sedaghati R. Neural-network-based sliding-mode control of an uncertain robot using dynamic model approximated switching gain. IEEE Transactions on Cybernetics, 2021, 51(5): 2339–2346
42. Bagheri F, Komurcugil H, Kukrer O, Guler N, Bayhan S. Multi-input multi-output-based sliding-mode controller for single-phase quasi-Z-source inverters. IEEE Transactions on Industrial Electronics, 2020, 67(8): 6439–6449
43. Peng H J, Li F, Liu J G, Ju Z J. A symplectic instantaneous optimal control for robot trajectory tracking with differential-algebraic equation models. IEEE Transactions on Industrial Electronics, 2020, 67(5): 3819–3829
44. Rayguru M M, Mohan R E, Parween R, Yi L, Le A V, Roy S. An output feedback based robust saturated controller design for pavement sweeping self-reconfigurable robot. IEEE/ASME Transactions on Mechatronics, 2021, 26(3): 1236–1247
45. Yadav R D, Sankaranarayanan V N, Roy S. Adaptive sliding mode control for autonomous vehicle platoon under unknown friction forces. In: Proceedings of the 20th International Conference on Advanced Robotics. Ljubljana: IEEE, 2021: 879–884
46. Wang D L, Wei W, Yeboah Y, Li Y J, Gao Y. A robust model predictive control strategy for trajectory tracking of omni-directional mobile robots. Journal of Intelligent & Robotic Systems, 2020, 98(2): 439–453
47. Zhang C Y, Chu D F, Liu S D, Deng Z J, Wu C Z, Su X C. Trajectory planning and tracking for autonomous vehicle based on state lattice and model predictive control. IEEE Intelligent Transportation Systems Magazine, 2019, 11(2): 29–40
48. Liang X W, Wang H S, Liu Y H, You B, Liu Z, Chen W D. Calibration-free image-based trajectory tracking control of mobile robots with an overhead camera. IEEE Transactions on Automation Science and Engineering, 2020, 17(2): 933–946
49. Ben Jabeur C, Seddik H. Design of a PID optimized neural networks and PD fuzzy logic controllers for a two-wheeled mobile robot. Asian Journal of Control, 2021, 23(1): 23–41
50. Xiong R, Li L J, Zhang C X, Ma K, Yi X S, Zeng H S. Path tracking of a four-wheel independently driven skid steer robotic vehicle through a cascaded NTSM-PID control method. IEEE Transactions on Instrumentation and Measurement, 2022, 71: 1–11
51. Lin H, Yin Y F, Shen X N, Alcaide A M, Liu J X, Leon J I,

Vazquez S, Franquelo L G, Wu L G. Fuzzy logic system-based sliding-mode control for three-level NPC converters. IEEE Transactions on Transportation Electrification, 2022, 8(3): 3307–3319
52. Mei K, Ding S H, Zheng W X. Fuzzy adaptive SOSM based control of a type of nonlinear systems. IEEE Transactions on Circuits and Systems II: Express Briefs, 2022, 69(3): 1342–1346
53. Lan Y P, Li J, Zhang F G, Zong M. Fuzzy sliding mode control of magnetic levitation system of controllable excitation linear synchronous motor. IEEE Transactions on Industry Applications, 2020, 56(5): 5585–5592
54. Lu Y Y, Zhang W. A piecewise smooth control-Lyapunov function framework for switching stabilization. Automatica, 2017, 76, 258–265
55. Mozayan S M, Saad M, Vahedi H, Fortin-Blanchette H, Soltani M. Sliding mode control of PMSG wind turbine based on enhanced exponential reaching law. IEEE Transactions on Industrial Electronics, 2016, 63(10): 6148–6159
56. Orozco-Magdaleno E C, Gómez-Bravo F, Castillo-Castañeda E, Carbone G. Evaluation of locomotion performances for a mecanum-wheeled hybrid hexapod robot. IEEE/ASME Transactions on Mechatronics, 2021, 26(3): 1657–1667
57. Ulrich I, Borenstein J. VFH+: reliable obstacle avoidance for fast mobile robots. In: Proceedings of 1998 IEEE International Conference on Robotics and Automation. Leuven: IEEE, 1998, 2: 1572–1577